A novel dynamic aeroelastic framework for aeroelastic tailoring and structural optimisation

Werter, Noud; De Breuker, Roeland

DOI
10.1016/j.compstruct.2016.09.044

Publication date
2016

Document Version
Accepted author manuscript

Published in
Composite Structures

Citation (APA)
Werter, N., & De Breuker, R. (2016). A novel dynamic aeroelastic framework for aeroelastic tailoring and structural optimisation. *Composite Structures*, *158*, 369–386. https://doi.org/10.1016/j.compstruct.2016.09.044

A novel dynamic aeroelastic framework for aeroelastic tailoring and structural optimisation[☆]

N.P.M. Werter[a,1,*], R. De Breuker[a,2]

[a]*Delft University of Technology, Faculty of Aerospace Engineering, Aerospace Structures and Computational Mechanics, Kluyverweg 1, 2629 HS, Delft, the Netherlands*

Abstract

Driven by a need to improve the efficiency of aircraft and reduce the fuel consumption, composite materials are applied extensively in the design of aircraft. A dynamic aeroelastic framework for the conceptual design of a generic composite wing structure is presented. The wing is discretized in several spanwise sections, where each section has a number of laminates throughout the cross-section, each having their own stiffness and thickness. The model uses a geometrically nonlinear beam model linearized around the nonlinear static aeroelastic equilibrium position coupled to a continuous-time state-space unsteady aerodynamic model to obtain the dynamic aeroelastic response, making the model suitable for dynamic aeroelastic analysis of generic aircraft wings under the assumption of small disturbances with respect to the static aeroelastic equilibrium position. Two optimisations are run for a generic aircraft wing under manoeuvre load conditions and aeroelastic, structural, and aerodynamic constraints: one, a quasi-isotropic wing to serve as a reference solution and two, a fully tailored wing clearly showing the benefit of aeroelastic tailoring and the use of the present framework for conceptual wing design.

Keywords:

Aeroelasticity, Aeroelastic tailoring, Structural optimisation

Nomenclature

$\mathbf{a}$	=	Laminate in-plane compliance matrix (m^2/N)
E	=	Young's modulus (GPa)
E_{11}	=	Longitudinal modulus (GPa)
E_{22}	=	Transverse modulus (GPa)

[☆]Part of this work has been presented in Werter, N.P.M., and De Breuker, R., 2015. Aeroelastic Tailoring and Structural Optimisation Using an Advanced Dynamic Aeroelastic Framework. International Forum on Aeroelasticity and Structural Dynamics 2015, St. Petersburg, Russia. IFASD-2015-137

[*]Corresponding author

Email address: n.p.m.werter@tudelft.nl (N.P.M. Werter)

[1]PhD Candidate

[2]Assistant Professor

F_i	=	Force in direction i (N)
G	=	Shear modulus (GPa)
G_{12}	=	Shear modulus (GPa)
h	=	Plunge displacement (m)
I	=	Inertia tensor (kgm^2)
$\mathbf{K}$	=	Stiffness matrix
l	=	Length (m)
m	=	Mass (kg)
$\mathbf{M}$	=	Mass matrix
M_i	=	Moment about axis i (Nm)
mA	=	Mass per unit length (kg/m)
$\mathbf{mQ}$	=	First mass moment tensor per unit length (kgm/m)
$\mathbf{mI}$	=	Mass inertia tensor per unit length (kgm^2/m)
$\mathbf{p}$	=	Structural degrees of freedom vector
$\mathbf{r}$	=	Distance vector (m)
$\mathbf{R}$	=	Rotation matrix (-)
t_{ply}	=	Ply thickness (mm)
$\mathcal{T}$	=	Kinetic energy (Nm)
u	=	Displacement (m)
$\mathbf{v}$	=	Velocity vector (m/s)
V_∞	=	Free stream velocity (m/s)
x	=	Position (m)
α	=	Angle of attack (deg)
γ	=	Shear strain (-)
Γ	=	Vortex strength (m^2/s)
ϵ	=	Normal strain (-)
$\boldsymbol{\theta}$	=	Total rotation pseudovector(-)
ν_{12}	=	Poisson's ratio (-)
ξ_i	=	Lamination parameter i (-)
ρ	=	Density (kg/m^3)

1. Introduction

Driven by a need to improve the efficiency of aircraft and reduce the fuel consumption, composite materials are applied extensively in the design of aircraft. In addition to a high specific strength and

stiffness, they also offer the designer the freedom to tailor the stiffness in desirable directions. One of the potential applications of this directional stiffness is aeroelastic tailoring, defined by Shirk et al.[1] as:

> *the embodiment of directional stiffness into an aircraft structural design to control aeroelastic deformation, static or dynamic, in such a fashion as to affect the aerodynamic and structural performance of that aircraft in a beneficial way.*

An extensive summary of early research on aeroelastic tailoring of swept and unswept wings has been written by Hertz et al.[2] Researchers have applied aeroelastic tailoring for different aspects of aircraft performance, for example, weight reduction of aircraft[3–5], gust load alleviation[6], improvement of flutter speed[7, 8] and drag reduction.[9] Furthermore, some research has been done on the effect of aeroelastic tailoring on the stability of supersonic aircraft[10], wings with external stores[11] and also in applications outside aerospace engineering.[12]

Early research performed by Librescu has focused on the aeroelastic tailoring of thin-walled beams,[13–15] which has more recently been extended by Qin et al. [10, 16]. The effect of variable stiffness along the span has been investigated by Dillinger et al.[17] using a shell model coupled to DLM in Nastran to do the static aeroelastic optimization of the top and bottom skin using lamination parameters and the laminate thickness. When looking at full wingbox tailoring including spars, Guo[5] investigates the effect of ply angles on the flutter speed of an aerobatic aircraft wing. The effect of linearly varying fibre angles on the aeroelastic response of a composite plate has been investigated by Stodieck et al.[18] and Stanford et al.[19] More recently, the use of a varying fibre angle on the top and bottom skin of the wing structure for aeroelastic tailoring has been investigated by several researchers.[20, 21] However, in order to comply with certification requirements and reduce the number of design variables, the fibre angles at each location were limited to 0 deg, 45 deg, -45 deg, and 90 deg and tailoring is achieved by varying the fraction of each of the discrete ply angles in the stacking sequence and varying the 0 deg direction by means of fibre steering, thus limiting the design space a priori.

When looking at aeroelastic optimization, several optimization procedures have been applied to find the optimum layup for different objectives. Research has mainly focused on the use of a genetic algorithm for the optimization.[19, 22–24] The main disadvantage of genetic algorithms is that they require a significant amount of function evaluations to find the optimum, especially when a large design space is considered. Guo[5] uses a gradient-based optimizer to optimize the wingbox fibre angles for a constant thickness, while Dillinger et al.[17] combine stiffness and thickness optimization, but only considers the top and bottom skin and do not include dynamic aeroelasticity. Recently, several researchers[20, 21, 25] have used a gradient-based optimiser with adjoint sensitivities to optimise a combination of laminate thickness and the fraction of 0 deg, 45 deg, -45 deg, and 90 deg plies in the stacking sequence. Stanford et al.[20] optimised the wing structure for minimum weight under manoeuvre load conditions and a flutter constraint for balanced

and unbalanced laminates, and straight and steered fibres clearly illustrating the potential of aeroelastic tailoring for wing weight reduction. Similar results were obtained by Brooks et al.[21] for minimum fuel burn under manoeuvre and gust load conditions for both straight and steered fibres. Finally, Kennedy et al.[25] used only straight fibres to obtain a Pareto front of fuel burn versus wing weight under manoeuvre load conditions, also clearly showing the benefits of aeroelastic tailoring. However, in each of these cases the choice of discrete ply angles limits the composite design space a priori.

Within this field, the current paper describes the application of an aeroelastic analysis tool developed at the Delft University of Technology for the conceptual design of the wing box structure by means of aeroelastic tailoring. The model extends the current state-of-the-art by (i) combining stiffness and thickness optimization of the complete wingbox, (ii) including (eccentric) non-structural masses (e.g. the engine or main landing gear), and (iii) including dynamic aeroelastic constraints, while using a gradient-based optimiser for computational efficiency and lamination parameters not to restrict the design space a priori to a fixed set of ply angles. The framework also shows the implementation of a novel unsteady aerodynamic model based on the unsteady vortex lattice method written in continuous-time state-space that allows for a fast and efficient analysis of the unsteady aerodynamics around aircraft wings without requiring a transformation to the frequency domain and back.[26]

The proposed paper demonstrates the implementation of this dynamic aeroelastic framework including the implementation of external forces and non-structural masses, as is explained in sections 2 to 5. Finally the framework is applied to the optimisation of the one engine reference model (OERM) under manoeuvre load conditions, courtesy of DLR, showing the potential of the proposed framework for the structural optimisation of composite wings, as explained in section 6.

2. Modelling approach

The goal of the dynamic aeroelastic analysis and optimisation framework is to improve the conceptual design of aircraft wings by including aeroelasticity. Therefore, one of the key requirements of the framework is computational efficiency. For this purpose, the three-dimensional wing geometry is split in several spanwise sections, each having its own skin laminate distribution throughout the wing cross-section. These laminates are described using lamination parameters and the laminate thickness, since these define any composite laminate using a fixed number of continuous design variables, allowing for the use of more efficient, gradient-based optimisers.

The aeroelastic analysis and optimisation loop is depicted in Fig. B.1, and starts with the definition of the wing geometry and load cases as inputs to the loop. Next, the composite laminate properties that are used for the wing skins and spars are determined based on the material properties given as input and the lamination parameters and thicknesses generated by the optimiser. In order to generate the beam model,

these laminate properties, together with the cross-sectional geometry, are used to generate the Timoshenko cross-sectional stiffness matrix with respect to the beam reference axis, using the cross-sectional modeller developed by Ferede and Abdalla[27] For completeness, a brief overview of this procedure will be given in section 3.

As a third step, a geometrically nonlinear static aeroelastic analysis is carried out to obtain the nonlinear static displacement field of the aircraft for the various load cases. The static aeroelastic model is based on the work of De Breuker et al.[28], who coupled a geometrically nonlinear Timoshenko beam model based on the co-rotational formulation to the steady aerodynamic model developed by Weissinger[29] based on the distribution of horseshoe vortices along the wing span. In order to make this model suitable for the analysis of generic composite aircraft wings, the effect of external non-aerodynamic forces and wing camber still needed to be incorporated. In order to account for the effects of gravity of both the structural and non-structural masses and for the effect of engine thrust, the model is extended with the implementation of eccentric follower and non-follower forces based on the same co-rotational formulation already used for the structural model. Second, the effects of camber are accounted for by using an aerodynamic model based on the vortex lattice method instead of the Weissinger method. A brief description of the original model, followed by a description of the implementation of external, non-aerodynamic forces and the vortex lattice aerodynamic model is given in section 4.

As a final analysis step, a linear dynamic aeroelastic analysis is carried out around the nonlinear static equilibrium solution. The nonlinear structural stiffness matrix, obtained from the static analysis is linearised and coupled to a linear mass matrix to obtain the dynamic structural model. This model is then coupled to an unsteady aerodynamic model based on the unsteady vortex lattice method.[26] Using the linear dynamic analysis, the flutter speed is calculated, and dynamic displacements can be obtained under e.g. gust loads. A detailed description of the dynamic aeroelastic model is given in section 5.

The strains in the three-dimensional wing structure are retrieved in a post-processing step by using the cross-sectional modeller to convert the beam strains and curvatures to the skin strains. A brief description of this procedure is given in section 3.

Finally the static and dynamic responses, and the skin strains are then fed into the optimiser as objective or constraint and a gradient based optimiser is used to update the set of lamination parameters and thickness until a converged solution is found.

3. Cross-sectional modeller

The cross-sectional modeller, as mentioned in the modelling approach, has two functions in the optimisation loop. First, the cross-sectional properties have to be determined from the three dimensional wing model to obtain the equivalent one-dimensional properties. For this purpose a thin-walled cross-sectional

modeller was developed by Ferede and Abdalla.[27] The cross-section is discretized using linear Hermitian shell elements having constant properties and can be any arbritrary open or closed, thin-walled, composite cross-section. Using a variational asymptotic approach, the Timoshenko cross-sectional stiffness matrix and the cross-sectional mass properties can be determined.

Second, once the aeroelastic analysis has been completed, the cross-sectional modeller is used to recover the skin strains throughout the cross-section from the one-dimensional beam strains, to be able to assess potential skin failure and structural stability. These skin strains include both the Euler-Bernouilli strains and the second-order free warping solution.

4. Static aeroelastic framework

Once the cross-sectional properties have been determined, the static aeroelastic model can be defined. The static aeroelastic analysis module is based on the work of De Breuker et al.[28]

4.1. Structural model

The structural model is a finite element beam model using linear Timoshenko beam elements. The elements are coupled in a co-rotational framework to obtain a geometrically nonlinear structural solution. First, in order to verify the link between the cross-sectional modeller and the structural model, the present nonlinear structural model is compared to experiments carried out by Chandra et al.[30] for the structural response of anisotropic composite box beams. As an example, the beam with properties as given in Table B.1 will be used, to validate the present approach. The resulting comparison of the present approach to the experimental results and the different beam modelling approaches is shown in Fig. B.2. As can be seen, the present approach shows satisfactory agreement with the experimental results, and performs excellent compared to the other numerical approaches, thus validating the present approach.

In order to extend this model to account for the effects of gravity of both the structural and non-structural masses and for the effect of engine thrust, both constant and follower eccentric forces and moments have been implemented using a co-rotational formulation based on the work of Battini and Pacoste.[33]

Consider an eccentric node at location, $\mathbf{x_e}$, which is attached through a rigid link to $\mathbf{x_a}$, which is located on element k, as shown in Fig. B.3a. In order to link $\mathbf{x_e}$ to $\mathbf{x_a}$, an eccentricity vector $\mathbf{v_0}$ is defined, such that:

$$\mathbf{x_e} = \mathbf{x_a} + \mathbf{v_0} \tag{1}$$

Using the principal of virtual work and considering that the work done by the eccentric force vector should be equal to the work done by the equivalent nodal force vector, a relation can be derived between the

eccentric force vector, $\mathbf{F_e}$, and the equivalent nodal force vector, $\mathbf{F}$, as derived in the appendix, resulting in:

$$\mathbf{F} = \mathbf{H^T B_{ex}^T F_e} \tag{2}$$

The corresponding stiffness matrix is defined by:

$$\boldsymbol{\delta F} = \mathbf{K_e} \boldsymbol{\delta p} \tag{3}$$

and can be derived by taking the variation of equation (2), resulting in three different contributions to the total stiffness matrix. The first contribution comes from the variation of $\mathbf{H}$ and is commonly called the geometric moment stiffness, the second contribution comes from the variation of $\mathbf{B_{ex}}$ and is commonly the geometric rotation stiffness, and the final contribution comes from the variation of the external force vector and is commonly called the material stiffness. Note that the final contribution will only be non-zero in case of follower forces and moments.

In order to verify the implementation of external non-aerodynamic forces, the structural response of the present model is compared to a test case taken from Bathe and Bolourchi[34], as shown in Fig. B.4a. The corresponding beam properties and loads are given in Table B.2. First, the resulting tip location after deformation under a constant tip load is compared to results in literature and, as can be concluded from Table B.3, shows excellent agreement. Next, in order to verify the implementation of eccentric external forces and moments, the tip load is shifted, as indicated in Fig. B.4b, and the results are compared to Abaqus, since to the best of the authors knowledge, no results are available in the literature. As can be seen in Fig. B.5, the resulting out-of-plane displacement and rotation about the $y-$axis shows excellent agreement with Abaqus for both a constant direction and follower force and moment.

4.2. Aerodynamic model

The aerodynamic model is a linear model based on potential flow theory implemented using the vortex lattice method. The wing is modelled under a thin wing assumption, where the camber surface is discretised in chordwise and spanwise direction by means of vortex ring elements. The aerodynamic mesh is composed of rigid airfoils distributed spanwise, each represented by a camber line, of which the locations are updated based on the local structural deformations. The flow is assumed to be inviscid and irrotational, and compressibility is accounted for by means of the Prandtl-Glauert transformation. An excellent description of the modelling of aircraft wings by means of vortex ring elements is given by Katz and Plotkin.[36] The aerodynamic forces computed per panel are first transferred to the structural beam by means of a rigid link, after which the forces are converted into statically equivalent nodal forces, as is illustrated in Fig. B.6.

4.3. Aeroelastic model

The final wing discretisation, including both the structural and aerodynamic discretisation, is given in Fig. B.7. The structural and aerodynamic model are closely coupled and the geometrically nonlinear solution is obtained by using load control and the Newton-Raphson root finding method, where next to the structural stiffness matrix and the stiffness matrix introduced by non-aerodynamic external forces, the aerodynamic stiffness matrix required to find the geometrically nonlinear static aeroelastic solution is obtained by analytical derivation. Each iteration the aerodynamic mesh is updated based on the latest structural deformations, a new force vector introduced by the non-aerodynamic forces is determined, the structural deformations are updated based on the latest aerodynamic and non-aerodynamic forces, and the stiffness matrices are updated until a converged solution is found.

As a final verification of the geometrically nonlinear static aeroelastic model, the present approach is compared to the results obtained by Murua et al.[37] for a HALE aircraft wing with properties given in Table B.4. The geometrically nonlinear tip deflection at an angle of attack of 2 deg and 4 deg at a flight speed of 25 m/s with an air density of $0.0889\,\mathrm{kg/m^3}$ is shown in Fig. B.8, showing excellent agreement, thus verifying the static aeroelastic model.

5. Dynamic aeroelastic framework

The static aeroelastic model is extended with a dynamic aeroelastic model that allows for the analysis of the dynamic aeroelastic response of the wing to, for example, a gust. A linear dynamic aeroelastic analysis is carried out around the nonlinear static equilibrium solution to obtain the dynamic response of the wing and to be able to assess the aeroelastic stability of the wing.

5.1. Structural model

The dynamic structural model is based on the same linear Timoshenko beam elements as used for the static aeroelastic analysis. The nonlinear stiffness matrix obtained in the static aeroelastic analysis is linearised around the static equilibrium position and combined with a linear mass matrix to obtain the structural model. The mass matrix is derived from the kinetic energy of the Timoshenko beam elements, given by:[38, 39]

$$\mathcal{T} = \frac{1}{2}\int_{\mathcal{V}} \rho \mathbf{v}^{\mathbf{T}}\mathbf{v} d\mathcal{V}, \tag{4}$$

where ρ is the mass density and $\mathbf{v}$ is the local velocity vector. The local velocity vector can be related to the velocity and angular velocity of the beam reference axis, through:

$$\mathbf{v} = \dot{\mathbf{u}} + \dot{\boldsymbol{\theta}} \times \mathbf{r} \tag{5}$$

where $\mathbf{r}$ is the distance vector of the mass of the beam with respect to the beam reference axis. Introducing the cross-sectional properties, equation (4) can now be rewritten in terms of the local degrees of freedom and the cross-sectional properties as:

$$\mathcal{T} = \frac{l_o}{2} \int_0^1 mA\dot{\mathbf{u}} \cdot \dot{\mathbf{u}} + \dot{\mathbf{u}}^{\mathbf{t}}\mathbf{mQ}\dot{\boldsymbol{\theta}} + \dot{\boldsymbol{\theta}}^{\mathbf{T}}\mathbf{mI}\dot{\boldsymbol{\theta}} d\xi \tag{6}$$

where mA is the mass per unit length, $\mathbf{mQ}$ contains the first mass moments per unit length with respect to the beam reference axis, $\mathbf{mI}$ is the mass inertia tensor per unit length with respect to the beam reference axis, and ξ is the normalised position along the beam, x/l_0. The local element mass matrix is given by the Hessian of the kinetic energy with respect to the local degrees of freedom. The global mass matrix can be obtained by transforming the local mass matrices from local to global (deformed) coordinates and using standard FEM approaches to assemble the global mass matrix from the local element matrices, resulting in the following dynamic structural model:

$$\mathbf{M}\ddot{\mathbf{p}} + \mathbf{K}\mathbf{p} = \mathbf{F} \tag{7}$$

where $\mathbf{p}$ contains the structural degrees of freedom. In order to account for eccentric, non-structural masses, similarly the kinetic energy of the external mass is derived. Consider an external mass at location $\mathbf{x_e}$, similar to Fig. B.3a. Its kinetic energy is evaluated at the center of mass, such that no coupling exists between the translational and angular velocity of the external mass, resulting in:

$$\mathcal{T}_e = \frac{1}{2} m_e \mathbf{v_e^T} \mathbf{v_e} + \frac{1}{2} \dot{\boldsymbol{\theta}}_\mathbf{e}^\mathbf{T} \mathbf{I_e} \dot{\boldsymbol{\theta}}_\mathbf{e} \tag{8}$$

where m_e is the mass of the external mass, $\mathbf{v_e}$ is the velocity vector of the center of mass of the external mass, $\dot{\boldsymbol{\theta}}_\mathbf{e}$ is the angular velocity vector of the external mass, and $\mathbf{I_e}$ is the inertia tensor of the external mass with respect to its center of gravity. In order to relate the degrees of freedom of the external mass to the structural degrees of freedom, its location $\mathbf{x_e}$ is projected orthogonally onto the closest structural element, as already indicated in Fig. B.3a, resulting in the following relations:

$$\mathbf{v_e} = \mathbf{v_a} + \dot{\boldsymbol{\theta}}_\mathbf{a} \times \mathbf{r_e} \tag{9}$$

$$\dot{\boldsymbol{\theta}}_\mathbf{e} = \dot{\boldsymbol{\theta}}_\mathbf{a} \tag{10}$$

Similar to the implementation of the external forces, the degrees of freedom of point a can be related to the local element degrees of freedom and the local external mass matrix is then given by the Hessian of the kinetic energy with respect to the local degrees of freedom. The global external mass matrix can then be assembled by standard FEM approaches.

In order to verify the implementation of the linear mass matrix and the effect of the external masses, the model as described by Bathe and Bolourchi[34], that was also used to verify eccentric loads, has been extended with an eccentric tip mass, as specified in Table B.2 and Table B.5. The eccentric mass location is defined by Fig. B.4b. First, three different eccentric loads are applied to simulate a (non)linear static equilibrium solution, namely a force of 0 N (Linear), 75 N, and 150 N. Next, a dynamic simulation is carried out around the static equilibrium solution under a time dependent tip load, defined by:

$$F_{tip}(t) = 1000 \cdot \sin(2t)$$

The resulting time responses for different static equilibrium positions are given in Fig. B.9 and compared to the results obtained from Abaqus. As can be expected, in case no tip loads are applied, both models show good agreement, thus verifying the implementation of the linear mass matrix. However, as the level of nonlinearity increases, the difference between the fully nonlinear implementation in Abaqus and the quasi nonlinear implementation used in the present model increases. It should be noted, however, that for a tip load of 75 N, the tip deflection is already 16%, while the results still show good agreement. The corresponding structural frequencies show a maximum error in the first 10 eigenfrequencies of 0.3% in case no tip load is applied, 4.8% for a tip load of 75 N, and 7.8% for a tip load of 150 N, thus also showing good agreement up to a tip load of 75 N. Therefore, for general aircraft wings, the present model is expected to predict the dynamic behaviour adequately; however, care should be taken for extremely flexible aircraft wings. Furthermore, when considering the dynamic aeroelastic stability, the present model is expected to give a conservative approximation of the stability boundaries, since geometric structural nonlinearity introduces structural damping[40], which is not taken into account in the present model.

5.2. Aerodynamic model

The unsteady aerodynamic model that is coupled to the structural model is based on potential flow theory implemented by means of the unsteady vortex lattice method. A detailed explanation of the unsteady aerodynamic model used in the present approach is given in Werter et al.[26] A brief explanation will be included here for completeness. The wing is modelled as a thin wing and represented by its deformed camber surface. The wake is assumed to be flat and leaves the trailing edge in the free-stream direction. Since, in case of unsteady aerodynamics, the wake vorticity is no longer constant, both the wing surface and the wake surface are discretised, resulting in a discretisation as illustrated in Fig. B.10. Under the assumption of small perturbations with respect to the steady state and by applying the flow-tangency condition, the Kutta condition and Helmholtz theoreom for the transport of vorticity in the wake, the unsteady aerodynamic model can be written as a continuous-time state-space model:

$$\begin{bmatrix} \dot{\mathbf{\Gamma}}_\mathbf{w} \\ \dot{\boldsymbol{\alpha}} \end{bmatrix} = \begin{bmatrix} \mathbf{K_1} & \mathbf{K_2} \\ \mathbf{0} & \mathbf{0} \end{bmatrix} \begin{bmatrix} \mathbf{\Gamma}_\mathbf{w} \\ \boldsymbol{\alpha} \end{bmatrix} + \begin{bmatrix} \mathbf{0} \\ \mathbf{I} \end{bmatrix} \dot{\boldsymbol{\alpha}} \tag{11}$$

$$\mathbf{F_a} = \begin{bmatrix} \mathbf{L_1} & \mathbf{L_2} \end{bmatrix} \begin{bmatrix} \mathbf{\Gamma}_\mathbf{w} \\ \boldsymbol{\alpha} \end{bmatrix} + \mathbf{L_3}\dot{\boldsymbol{\alpha}} \tag{12}$$

where $\mathbf{\Gamma_w}$ are the vortex strengths of the aerodynamic panels of the free wake panels and $\boldsymbol{\alpha}$ are the perturbation angles of attack of the aerodynamic panels on the wing surface. Once the vortex strength distribution in the free wake is resolved, the vortex strength distribution on the wing surface and in the trailing edge wake panels can be determined by inserting these in the equations for the flow tangency condition and the Kutta condition. The input of the state-space model is given by the time derivative of the perturbation angle of attack and is defined separately for each aerodynamic wing panel.

Compressibility has been accounted for by means of the Prandtl-Glauert transformation, which limits the applicability of the unsteady aerodynamic model to low to moderate compressible reduced frequencies and no shocks, so care should be taken in applying this model to a combination of high Mach number and high reduced frequency. However, within these limitations, the present model is still expected to provide a good approximation of the effect of compressibility on the unsteady aerodynamics. The effect of transonic aerodynamic effects could be included in future work, for example, by means of a correction of the unsteady aerodynamic loads by CFD simulations. The main advantage of the present model, however, is that it allows for efficient discrete gust simulations in time domain.

5.3. Aeroelastic model

In order to couple the structural and aerodynamic models, the aerodynamic forces need to be transferred to the structural nodes as input to the structural model and the time derivative of the perturbation angle of attack induced by the structural deformations on the aerodynamic panels needs to be determined as input to the unsteady aerodynamic model. Similar to the steady aerodynamic model, the aerodynamic forces are first transferred to the structural beam by means of a rigid link, and then converted into statically equivalent nodal forces, as is illustrated in Fig. B.6, resulting in the following transformation equation:

$$\mathbf{F_s} = \mathbf{T_{AS}}\mathbf{F_a} \tag{13}$$

The perturbation angle of attack on each aerodynamic panel is composed of four components:

$$\alpha = \alpha_{air} + \theta - \frac{\dot{h}}{V_\infty} + \frac{\dot{\theta}\,(x - x_b)}{V_\infty} \tag{14}$$

where α_{air} is the perturbance angle of attack induced by the free stream flow, θ is the structural wing twist, $-\frac{\dot{h}}{V_\infty}$ is the perturbance angle of attack introduced by the local plunge motion of the wing, and $\frac{\dot{\theta}(x-x_b)}{V_\infty}$

is the perturbance angle of attack introduced by the local pitch rate of the wing, where x defines the location of the aerodynamic panel and x_b defines the location of the beam axis. The local structural deformations are found by a linear interpolation of the nodal structural deformations to the spanwise aerodynamic stations, resulting in the following transformation equation for each of the structural translations, rotations, and velocities:

$$\mathbf{x_a} = \mathbf{T_{SA}}\mathbf{x_s} \tag{15}$$

where $\mathbf{x_s}$ contains translations, rotations or velocities at the structural nodes, and $\mathbf{x_a}$ contains the corresponding degrees of freedom at the aerodynamic spanwise stations.

Starting from the aerodynamic state-space system, as defined by equation (11) and equation (12), using equation (14), the aerodynamic state equation can be linked to the different components of the perturbation angle of attack. Similarly, using equation (13), the structural state-space system can be linked to the aerodynamic forces. Combining both relations the aeroelastic state equation, as derived in the appendix, is obtained as:

$$\dot{\mathbf{x}} = \mathbf{A_{ss}}\mathbf{x} + \mathbf{B_{ss}}\dot{\boldsymbol{\alpha}}_{\mathbf{air}} \tag{16}$$

where the state vector $\mathbf{x}$ is defined as:

$$\mathbf{x} = \begin{bmatrix} \boldsymbol{\Gamma}_{\mathbf{w}} & \boldsymbol{\alpha}_{\mathbf{air}} & \dot{\mathbf{p}} & \mathbf{p} \end{bmatrix}^T \tag{17}$$

In order to complete the dynamic aeroelastic state-space system, the aerodynamic forces and moments and the structural degrees of freedom are selected as outputs, resulting in the following output equations, as derived in the appendix:

$$\begin{bmatrix} \mathbf{F} \\ \mathbf{p} \end{bmatrix} = \mathbf{C_{ss}}\mathbf{x} + \mathbf{D_{ss}}\dot{\boldsymbol{\alpha}}_{\mathbf{air}} \tag{18}$$

In order to verify the dynamic aeroelastic model, first the flutter speed for the Goland wing[41], as given in Table B.6, and the HALE aircraft wing, as given in Table B.4, are compared to the literature. The flutter speed is determined by increasing the velocity until the eigenvalues of the state matrix $\mathbf{A_{ss}}$ become unstable, i.e. until the real part of one of the eigenvalues becomes positive. As can be seen in Table B.7, the results show excellent agreement.

Second, in order to validate the implementation of the eccentric masses, the aeroelastic stability as predicted by the present model is compared to the experimental results of Runyan and Sewall.[44] The wing properties are given in Table B.8 and the comparison is shown in Fig. B.11. When looking at the results, several things can be observed. First of all, the predicted flutter and divergence speeds show excellent

agreement with the experiments, however, both the present model and Fazelzadeh et al.[45] overpredict the flutter frequency by $10-15\%$, which can probably be explained by inaccuracies between the modelling of the experiment and the actual experiment. Second, the present model predicts transition from flutter to divergence already at 0.406 m, while in the experiment the wing was close to divergence, but still fluttering. In general, however, the present results show good agreement with the experiments, thus validating the implementation of eccentric masses in the present model.

Finally, to verify the implementation of gust in the present model, the results obtained for a gust analysis of the Goland wing, as already given in Table B.6, under a 1-cosine gust are compared to results obtained by Wang et al.[46] The air density is $1.229\,\mathrm{kg/m^3}$ and the mean free-stream flow velocity is 100 m/s. The discrete gust has an amplitude of $V_G/V = 0.001$ and a length of $L_G = 4$ chords. The resulting tip deflection and tip twist are shown in Fig. B.12. As can be expected, both results show excellent agreement, since both models are based on a beam model coupled to a UVLM-based model.

In conclusion, the present model shows excellent agreement with results found in the literature, thus verifying and validating the present dynamic aeroelastic model. Note that, for optimisation purposes, the framework not only produces the aeroelastic responses, but also the sensitivities of the responses with respect to the lamination parameters and laminate thicknesses. All sensitivities are computed analytically for computational efficiency.

6. Aeroelastic tailoring of the OERM

In order to assess the use of the present model for conceptual design and assess the potential of aeroelastic tailoring, the present model is applied to the stiffness and thickness optimisation of a wing designed for large civilian aircraft, courtesy of DLR, the German Aerospace Research Center, that is referred to as the One Engine Reference Model (OERM). The aircraft has a wing span of 58.0 m, leading edge sweep of 31.8 deg, and a wing surface area of $380\,\mathrm{m^2}$. The wing planform and wing box dimensions are given in Fig. B.13a and Table B.9. The beam reference axis is placed at the wing quarter chord line, as indicated in Fig. B.13a. The corresponding spanwise twist distribution is given in Fig. B.13b. The aircraft mass excluding the wing, and any nonstructural masses on the wing, is 90 000 kg.

The wing has 41 equally spaced ribs that are taken into account as concentrated masses to account for their effect on the wing mass distribution. The stiffening effect of the ribs on the cross-section is inherently taken into account in the beam model under the assumption of a rigid cross-section. The stiffening effect caused by the warping restraint introduced by the ribs, however, has been neglected in the present model. The properties of the engine, pylon and main landing gear are given in Table B.10 and they are also accounted for as concentrated masses. Finally, the wing fuel distribution is taken into account by including 5 fuel tanks as specified by Table B.11 and Fig. B.13d. The fuel level in the different tanks is accounted for by changing

the mass of the fuel accordingly. The corresponding location of the different fuel masses is given in Fig. B.13c.

6.1. Optimisation approach

In order to assess the potential of aeroelastic tailoring, two optimisations are run: one, a thickness optimisation of a quasi-isotropic composite wing which will serve as a reference solution and, two, a complete thickness and stiffness optimisation of a composite wing to show the effect of stiffness optimisation on wing design. Table B.12 shows the material properties used throughout the optimisation. A brief overview of the optimisation setup is given in Table B.13.

The objective of the optimisations is to minimise structural weight. The wing is split in 16 spanwise sections: one section covering the area between the wing root and the first kink, three equally spaced sections covering the area between the first and the second kink, and 12 equally spaced sections covering the area between the second kink and the wing tip. Each section consists of four material sections, top and bottom skin, and the leading edge and trailing edge spar, or in case of the presence of a mid spar, five material sections.

In case of the quasi-isotropic wing, the design variables are the thicknesses of different material patches along the wing. In case of the aeroelastically tailored wing, the design variables consist of eight lamination parameters, describing the in-plane and out-of-plane behaviour of the composite laminates, and the thickness per material section. For manufacturing reasons, the laminates are assumed to be symmetric, thus no coupling exists between the in-plane behaviour and the out-of-plane behaviour of the laminates. The laminates are described using lamination parameters, since these have several advantages over the use of ply angles when used in an optimisation process. First of all, any laminate, independent of the number of plies, can be described by a fixed number of parameters, in this case eight to describe the thickness normalized stiffness and one to include thickness, thus reducing the number of design variables required in the optimisation. Secondly, lamination parameters are continuous variables, thus allowing for the use of a gradient-based optimiser to speed up convergence of the optimisation process. In order to ensure that the combination of lamination parameters corresponds to an actual laminate, the following constraints are set on the lamination parameters:[47]

$$2\left(\xi_1\right)^2\left(1-\xi_2\right)+2\left(\xi_3\right)^2\left(1+\xi_2\right)+\left(\xi_2\right)^2+\left(\xi_4\right)^2-4\xi_1\xi_3\xi_4\leq 1 \tag{19}$$

$$\left(\xi_1\right)^2+\left(\xi_3\right)^2\leq 1 \tag{20}$$

$$-1\leq\xi_i\leq 1 \tag{21}$$

where the same constraints apply for both the in-plane and out-of-plane lamination parameters. Note that, in reality the in-plane and out-of-plane stiffness components cannot be varied independently, and

additional constraints are required to fully define the lamination parameter domain. In order to approximate the full feasibility region of lamination parameters, two approaches exist in the literature. Bloomfield et al.[48] obtained a set of constraints describing the convex hull of the lamination parameter design space by considering a set of predefined ply angles and Setoodeh et al.[49] obtained a set of linear constraints by approximating the convex hull of the lamination parameter design space by generating feasible design points until the total volume of the convex hull has converged. Both approaches have not been considered in the present paper, since the approach by Bloomfield et al.[48] constrains the design space a priori to a set of fixed ply angles, negating one of the benefits of the use of lamination parameters and the approach by Setoodeh et al.[49] results in a large amount of constraints (i.e. 37126 for the combination of $\xi_{1\mathbf{A}}$, $\xi_{3\mathbf{A}}$, $\xi_{1\mathbf{D}}$, and $\xi_{3\mathbf{D}}$) slowing down the optimisation process.

More recently Wu et al.[50] used the Schwarz inequality to derive an expression linking $\xi_{1\mathbf{A}}$, $\xi_{2\mathbf{A}}$ and $\xi_{1\mathbf{D}}$, resulting in a necessary, but not sufficient constraint equation linking the A- and D-matrix:

$$5\left(\xi_{1\mathbf{A}}-\xi_{1\mathbf{D}}\right)^2-2\left(1+\xi_{2\mathbf{A}}-2\left(\xi_{1\mathbf{A}}\right)^2\right)\leq 0 \tag{22}$$

In the present optimisations strain is the main design driver, and, hence, the designs are dominated by the A-matrix, making this constraint inactive. For future problems, when, for example, buckling is accounted for and the D-matrix becomes important, this constraint could, however, become active and should be accounted for to improve the match between the optimised lamination parameter results and actual stacking sequence results.

In general, a slightly reduced performance is expected when converting the lamination parameters to an actual stacking sequence; however, most panels will only be critical in either in-plane behaviour (A-matrix) or out-of-plane behaviour (D-matrix), allowing for a sacrifice in performance of the non-critical response in favour of the critical response.

Other manufacturing considerations, such as the 10% rule, ply drop rate, or maximum number of plies of the same orientation next to each other, have not been considered in the present paper. The focus of this paper is on the potential increase in performance by using composites for aeroelastic tailoring and will only address the continuous stiffness optimisation leaving the conversion of the continuous optimum to a discrete stacking sequence including manufacturing constraints for future work. For all optimisations, the thickness is limited between 1 mm and 50 mm.

In order to ensure a feasible final design, constraints are set on the aeroelastic stability, the local angle of attack and the strains. As explained in section 5, the aeroelastic stability is governed by the eigenvalues of the state matrix, resulting in the following constraint on the real part of the eigenvalues for aeroelastic

stability of the wing:

$$\Re(\lambda) \leq 0 \tag{23}$$

The local angle of attack is defined by the aircraft angle of attack, the local wing twist, and the twist induced by the structure, and is limited to ± 12 deg to ensure attached aerodynamic flow, while still leaving design freedom to the optimiser. Finally, a constraint is set on the maximum principal strain, minimum principal strain, and maximum shear strain in the cross-section, as computed by the cross-sectional modeller, based on the material limits, as given in Table B.12.

Six load cases were selected based on the EASA CS25 regulations covering different parts of the flight envelope, as specified in Table B.14. Note that especially load case 4 is at the limit of applicability of the aerodynamic model, so care should be taken in interpreting the results. However, the model is still expected to provide a good approximation of the aeroelastic response of the wing and show the potential of aeroelastic tailoring for wing weight reduction. All analyses were done at a trimmed flight condition with the effects of gravity included.

The globally convergent method of moving asymptotes (GCMMA) developed by Svanberg[51] is used as a gradient-based optimiser. Direct sensitivities have been used and all sensitivities of the objective and constraints with respect to the design variables are obtained analytically.

In order to start the optimisation, a thickness distribution of 15 mm at the root increasing linearly to 25 mm at the engine location and then decreasing linearly to 8 mm at the tip is used as an initial design for both the skin and the spars, resulting in an initial weight of 6275 kg for both composite wings. All initial laminates are quasi-isotropic. Note that the initial design is a very heavy design and not representative of an actual wing design. Therefore, the initial design should not be used as a reference to evaluate the potential of aeroelastic tailoring. The potential of aeroelastic tailoring is assessed by directly comparing the optimisation results of the quasi-isotropic wing to the optimisation results of the tailored wing.

6.2. Quasi-isotropic wing

The final quasi-isotropic wing design is obtained after 50 iterations, resulting in an optimised weight of 2440 kg. The corresponding trim angles of attack at the start and end of the cruise are given in Table B.15. The evolution of weight and root bending moment as the optimisation progressed is given in Fig. B.14. As can be seen and expected, a reduction in weight is linked to a reduction in root bending moment, clearly indicating the importance of the root bending moment in wing design.

The optimised thickness distribution is given in Fig. B.15, showing an increase in skin thickness towards the engine location and then a reduction in skin thickness towards the tip. The design does not include stiffeners and, therefore, the final thickness distribution should be interpreted as the smeared thickness of an equivalent stiffened panel. It is interesting to note that the leading edge spar is significantly thicker than

the trailing edge spar around midspan, indicating a form of aeroelastic tailoring through thickness tailoring. As a result, the shear center shifts forward, resulting in an wash-out bend-twist coupling, as can be seen in Fig. B.16a. Finally this results in a lift distribution where lift is shifted inboard, as can be concluded from Fig. B.16b, thus reducing the root bending moment and resulting in a reduction in weight. It is interesting to note that at the root of the wing, the trailing edge spar is thicker than the leading edge spar and midspar because of the location of the main landing gear and the loads this introduces on the structure.

The final design is dominated by the normal strain constraints, as can be concluded from the strain results in Fig. B.17, Fig. B.18, and Fig. B.19. Results are presented for load case 3 ($-1g$) and load case 5 ($2.5g$), since these are the dominant load cases for the wing design. As can be expected, load case 5 is dominant for the minimal principal strain and shear strain in the top skin, for the maximum principal strain and shear strain in the bottom skin and the strains in the spars, while load case 3 is dominant for the maximum principal strain in the top skin and the minimal principal strain in the bottom skin. For each of the wing sections, the thickness is optimised such that the strain limit is reached.

In conclusion, although, for example, control reversal and panel buckling have not been accounted for, which might reduce the actual load alleviation that is obtained, the results clearly show the potential of aeroelastic tailoring and the load alleviation that can be achieved.

6.3. Tailored wing

Similar to the quasi-isotropic wing, the final fully tailored wing design is obtained after 50 iterations, resulting in an optimised weight of 1164 kg. The corresponding trim angles of attack at the start and end of the cruise are given in Table B.15 and the evolution of weight and root bending moment as the optimisation progressed is given in Fig. B.14. When comparing the fully tailored wing design to the quasi-isotropic wing design, a weight reduction of 52.3% is obtained. Note that the current optimisation setup does not include any buckling constraint, so care should be taken in interpreting this reduction in weight, since for very thin laminates buckling becomes critical instead of strength, however, this result clearly shows the potential of aeroelastic tailoring.

The optimised stiffness and thickness distribution is given in Fig. B.20, where the wing stiffness distribution is represented by a polar plot of the thickness-normalized modulus of elasticity for each laminate section. The polar plot of the thickness-normalised modulus of elasticity is obtained by computing the thickness-normalised laminate compliance matrix, $\hat{\mathbf{a}}$, at an angle θ from 0 to 360 deg and plotting the modulus of elasticity defined as:

$$\hat{E}_{11}(\theta) = \frac{1}{\hat{a}_{11}(\theta)} \tag{24}$$

Two spanwise sections can be identified when looking at the skin stiffness distribution: (i) from the root up to the engine location, and (ii) from the engine location up to the wing tip. The first section is dominated

by stiffness along the wing axis to provide sufficient stiffness to sustain all loads. Most classic aeroelastic tailoring can be seen in the second section, where the laminates introduce a bend-twist coupling to produce wing wash-out and thus shift the lift inboard, as can also be concluded when looking at the tailored twist distribution in Fig. B.16a and the lift distribution in Fig. B.16b. When looking at the wing spars, the effect of the main landing gear can clearly be observed at the wing root, resulting in increased torsional stiffness of the midspar and trailing edge spar. The remainder of the first section up to the engine is clearly dominated by ± 45 deg tailoring to increase shear stiffness and carry the loads introduced by the engine. In the second section, the leading edge spar is mainly dominated by ± 45 deg tailoring to increase shear stiffness, while the trailing edge spar is more flexible, thus inducing wash-out bend-twist coupling by shifting the shear center forward. In conclusion, the stiffness results clearly illustrate the importance of taking into account all important non-structural wing components (e.g. the engine or the main landing gear) and taking into account the wing spars to use aeroelastic tailoring to influence wing performance.

When looking at the wing thickness distribution, similar to the quasi-isotropic wing the skin thickness increases up to the engine location and then decreases to the wing tip, and the leading edge spar is significantly thicker than the trailing edge spar around the midspan, indicating a form of aeroelastic tailoring through thickness tailoring. In contrast to the quasi-isotropic wing, the final design is no longer only dominated by the normal strain constraints, but also by the shear strain constraints, as can be seen in Fig. B.17c, Fig. B.18c, and Fig. B.19c.

In conclusion, although care should be taken when interpreting the results, since control reversal and buckling are not included as a constraint and aerodynamic performance might impose a constraint on the wing lift distribution, the final optimised tailored wing, clearly shows the potential of aeroelastic tailoring and the power of the framework described in the present paper.

7. Conclusions

A dynamic aeroelastic framework for the conceptual design of a generic composite wing structure is presented. The wing is discretized in several spanwise sections, where each section has a number of laminates throughout the cross-section, each having their own stiffness and thickness. The laminates are described using lamination parameters to allow for the use of a gradient-based optimiser. The geometrically nonlinear static aeroelastic solution is obtained by coupling a geometrically nonlinear Timoshenko beam model to a vortex lattice aerodynamic model. Dynamic aeroelastic stability is assessed by a linear dynamic aeroelastic analysis around the geometrically nonlinear static equilibrium solution. Verification has shown good accuracy for tip deflection up to 15% and small gust angles, making the model suitable for general aircraft wings, however care should be taken when modelling highly flexible wings under large amplitude gusts. All relevant non-structural masses (e.g. the engine or the main landing gear) are accounted for in both the static and

dynamic aeroelastic analyses.

The framework has been applied to the optimization of a generic wing designed for large civilian aircraft under manoeuvre load conditions. Two optimizations were run: one, a quasi-isotropic wing where only thickness is optimized to act as a reference solution, and two, a fully tailored wing. Aeroelastic stability and principal strain limits were applied as constraints. The results clearly show the importance of taking into account all important non-structural wing components (e.g. the engine or the main landing gear) and taking into account the wing spars in the aeroelastic tailoring design process.

The optimised results show a potential reduction in weight of 52.3% of the tailored wing with respect to the quasi-isotropic wing. Although care should be taken when interpreting the results, since control reversal and buckling are not included as a constraint and aerodynamic performance might impose a constraint on the wing lift distribution, the final optimised tailored wing, clearly shows the potential of aeroelastic tailoring and the power of the framework described in the present paper.

Future work will focus on the introduction of a control reversal constraint and a buckling constraint, the investigation of aeroelastic tailoring under gust loads, and the investigation of the effect of transonic aerodynamic effects on the aeroelastic response. In conclusion, although further research is required, the final optimized tailored wing clearly shows the potential of aeroelastic tailoring and the power of the framework described in the present paper.

Acknowledgements

The authors would like to acknowledge the EU Joint Technology Initiative Clean Sky, Smart Fixed Wing Aircraft project for its contribution in funding this work and Lorenz Vandewaeter for his initial work on the implementation of eccentric forces and masses.

Appendix A. Derivation of the nodal force vector and stiffness matrix due to eccentric forces

Consider a eccentric node at location, $\mathbf{x_e}$, which is attached through a rigid link to $\mathbf{x_a}$, which is located on element k, as shown in Fig. B.3a. In order to link $\mathbf{x_e}$ to $\mathbf{x_a}$, an eccentricity vector $\mathbf{v_0}$ is defined, such that:

$$\mathbf{x_e} = \mathbf{x_a} + \mathbf{v_0} \tag{A.1}$$

Since $\mathbf{x_e}$ is attached to $\mathbf{x_a}$ through a rigid link, $\mathbf{v_0}$ is constant in the local element coordinate system. Therefore, if the rotation of the local element from its local coordinate system to the co-rotated coordinate system is defined through a rotation matrix, $\mathbf{R_a}$, the co-rotated eccentricity vector is given by:

$$\mathbf{v} = \mathbf{R_a v_0} \tag{A.2}$$

Using Fig. B.3b, the deformation of the eccentric node, $\mathbf{x_e}$, can now be related to the deformation of location, $\mathbf{x_a}$, resulting in:

$$\mathbf{u_a} + \mathbf{v} = \mathbf{v_0} + \mathbf{u_e} \tag{A.3}$$

$$\mathbf{u_e} = \mathbf{u_a} + (\mathbf{R_a} - \mathbf{I})\,\mathbf{v_0} \tag{A.4}$$

In order to obtain the nodal force vector and stiffness contribution introduced by the eccentric forces and moments, the principle of virtual work is used. A transformation between the eccentric force and moment vector and the nodal force vector can be obtained by considering that both forces should perform the same external virtual work:

$$\boldsymbol{\delta}\mathbf{p_e^T}\mathbf{F_e} = \boldsymbol{\delta}\mathbf{p^T}\mathbf{F} \tag{A.5}$$

with

$$\boldsymbol{\delta}\mathbf{p_e^T} = [\mathbf{u_e}, \boldsymbol{\theta}_\mathbf{e}] \tag{A.6}$$

$$\boldsymbol{\delta}\mathbf{p^T} = [\mathbf{u_1}, \boldsymbol{\theta_1}, \mathbf{u_2}, \boldsymbol{\theta_2}] \tag{A.7}$$

where $\boldsymbol{\theta_e}$ is the total rotational pseudovector of the eccentric node, $\mathbf{u_1}$ and $\mathbf{u_2}$ are the displacement vectors of node 1 and node 2, and $\boldsymbol{\theta_1}$ and $\boldsymbol{\theta_2}$ are the total rotational pseudovectors of node 1 and node 2 respectively. Therefore, in order to find the nodal force vector corresponding to the eccentric force and moment vector, the variation of the deformation of the eccentric node has to be related to the variation of the nodal deformations of the corresponding beam element. Taking the variation of equation (A.4), and recognizing that $\mathbf{v_0}$ is constant, the following relation is obtained for the variation of the displacements at the eccentric node:

$$\boldsymbol{\delta}\mathbf{u_e} = \boldsymbol{\delta}\mathbf{u_a} + \boldsymbol{\delta}\mathbf{R_a}\mathbf{v_0} \tag{A.8}$$

The variation of a rotation matrix is related to its spatial angular variations, $\boldsymbol{\delta\vartheta}$, through:

$$\boldsymbol{\delta}\mathbf{R_a} = \boldsymbol{\delta}\tilde{\boldsymbol{\vartheta}}_\mathbf{a}\mathbf{R_a} \tag{A.9}$$

where the tilde indicates the skew symmetric representation of a pseudo vector and the spatial angular variations represent an infinitesimal rotation superimposed on $\mathbf{R_a}$. Using $\mathbf{a\tilde{b}} = -\mathbf{b\tilde{a}}$ and introducing equation (A.2), the variation of the displacements at the eccentric node can be related to the variation of the deformations of point a through:

$$\boldsymbol{\delta}\mathbf{u_e} = \boldsymbol{\delta}\mathbf{u_a} - \tilde{\boldsymbol{v}}\boldsymbol{\delta\vartheta_a} \tag{A.10}$$

Recognizing that the rotations of the eccentric node are equal to the rotations of point a, the deformation vector of the eccentric node can be related to the deformations at point a through:

$$\boldsymbol{\delta}\mathbf{p_e} = \begin{bmatrix} \mathbf{I} & -\tilde{\boldsymbol{v}} \\ \mathbf{0} & \mathbf{I} \end{bmatrix} \begin{bmatrix} \boldsymbol{\delta}\mathbf{u_a} \\ \boldsymbol{\delta}\boldsymbol{\vartheta}_\mathbf{a} \end{bmatrix} \tag{A.11}$$

In order to relate the deformations of point a to the deformations of node 1 and node 2, a linear interpolation is used, resulting in the following relation for the eccentric deformations as a function of the global deformations of node 1 and node 2:

$$\boldsymbol{\delta}\mathbf{p_e} = \underbrace{\begin{bmatrix} (1-\xi)\,\mathbf{I} & -(1-\xi)\,\tilde{\boldsymbol{v}} & \xi\mathbf{I} & -\xi\tilde{\boldsymbol{v}} \\ \mathbf{0} & (1-\xi)\,\mathbf{I} & \mathbf{0} & \xi\mathbf{I} \end{bmatrix}}_{\mathbf{B_{ex}}} \underbrace{\begin{bmatrix} \boldsymbol{\delta}\mathbf{u_1} \\ \boldsymbol{\delta}\boldsymbol{\vartheta}_\mathbf{1} \\ \boldsymbol{\delta}\mathbf{u_2} \\ \boldsymbol{\delta}\boldsymbol{\vartheta}_\mathbf{2} \end{bmatrix}}_{\boldsymbol{\delta}\mathbf{p_g}} \tag{A.12}$$

where ξ is the normalised location of the rigid link along the beam element. Note that the spatial angular variation and the total rotational pseudovector are not additive. In order to make the rotational vectors additive, the spatial angular variation needs to be transformed to the variation of the total rotational pseudovector, through:

$$\boldsymbol{\delta\theta} = T_s\left(\boldsymbol{\theta}\right)\boldsymbol{\delta\vartheta} \tag{A.13}$$

as derived by Battini and Pacoste.[33] Introducing equation (A.13) in equation (A.12), the variations of the deformations of the eccentric node can be related to the variations of the nodal displacements, resulting in:

$$\boldsymbol{\delta}\mathbf{p_e} = \mathbf{B_{ex}}\left(\mathbf{p_g}\right)\mathbf{H}\left(\mathbf{p}\right)\boldsymbol{\delta}\mathbf{p} \tag{A.14}$$

where $\mathbf{H}\left(\mathbf{p}\right)$ is defined by:

$$\mathbf{H}\left(\mathbf{p}\right) = \begin{bmatrix} \mathbf{I} & & & \mathbf{0} \\ & T_s\left(\boldsymbol{\theta}_\mathbf{1}\right) & & \\ & & \mathbf{I} & \\ \mathbf{0} & & & T_s\left(\boldsymbol{\theta}_\mathbf{2}\right) \end{bmatrix} \tag{A.15}$$

Inserting equation (A.14) in equation (A.5), the following equation for the nodal force vector as a function of the eccentric force vector can now be found:

$$\mathbf{F} = \mathbf{H^T}\mathbf{B_{ex}^T}\mathbf{F_e}$$

The corresponding stiffness matrix is defined by:

$$\boldsymbol{\delta F} = \mathbf{K_e}\boldsymbol{\delta p} \tag{A.16}$$

and can be derived by taking the variation of equation (2), resulting in three different contributions to the total stiffness matrix. The first contribution comes from the variation of $\mathbf{H}$ and is commonly called the geometric moment stiffness, the second contribution comes from the variation of $\mathbf{B_{ex}}$ and is commonly called the geometric rotation stiffness, and the final contribution comes from the variation of the external force vector and is commonly called the material stiffness. Note that the final contribution will only be non-zero in case of follower forces or moments.

Appendix B. Derivation of the dynamic aeroelastic state-space system

Starting from the aerodynamic state-space system, as defined by equation (11) and equation (12), using equation (14), the aerodynamic state equation can be linked to the different components of the perturbation angle of attack, resulting in:

$$\begin{bmatrix} \dot{\boldsymbol{\Gamma}}_\mathbf{w} \\ \dot{\boldsymbol{\alpha}}_\mathbf{air} \end{bmatrix} = \begin{bmatrix} \mathbf{K_1} & \mathbf{K_2} & -\mathbf{K_2}\mathbf{B}_{\boldsymbol{\alpha}}\frac{1}{V_\infty} & \mathbf{K_2}\mathbf{B}_{\boldsymbol{\alpha}} & \mathbf{K_2}\mathbf{B_{pitch}} \\ \mathbf{0} & \mathbf{0} & \mathbf{0} & \mathbf{0} & \mathbf{0} \end{bmatrix} \begin{bmatrix} \boldsymbol{\Gamma}_\mathbf{w} \\ \boldsymbol{\alpha}_\mathbf{air} \\ \dot{\mathbf{h}}_\mathbf{a} \\ \boldsymbol{\theta}_\mathbf{a} \\ \dot{\boldsymbol{\theta}}_\mathbf{a} \end{bmatrix} + \begin{bmatrix} \mathbf{0} \\ \mathbf{I} \end{bmatrix} \dot{\boldsymbol{\alpha}}_\mathbf{air} \tag{B.1}$$

where $\mathbf{B}_{\boldsymbol{\alpha}}$ links the spanwise pitch angle distribution, $\boldsymbol{\theta}_\mathbf{a}$, and plunge distribution, $\dot{\mathbf{h}}_\mathbf{a}$, to the correct aerodynamic panels, and $\mathbf{B_{pitch}}$ transform the spanwise pitch rate, $\dot{\boldsymbol{\theta}}_\mathbf{a}$ to the local induced angle of attack. $\dot{\boldsymbol{\alpha}}_\mathbf{air}$ is selected as only external input to the state equation, since all other components are directly related to the structural degrees of freedom. Note that $\dot{\mathbf{h}}_\mathbf{a}$ is defined in the aerodynamic coordinate system, which is aligned with the free stream velocity vector, while the structural degrees of freedom are defined in a body-fixed coordinate system. Therefore, the plunge motion is related to the structural degrees of freedom, through:

$$\dot{\mathbf{h}}_\mathbf{a} = \dot{\boldsymbol{\delta}}_{\mathbf{z_a}} = -\sin\alpha_0 \cdot \dot{\boldsymbol{\delta}}^*_{\mathbf{x_s}} + \cos\alpha_0 \cdot \dot{\boldsymbol{\delta}}^*_{\mathbf{z_s}} \tag{B.2}$$

where α_0 is the free-stream angle of attack, $\boldsymbol{\delta}$ is a vector containing structural deformations and the * denotes the structural degrees of freedom interpolated at the spanwise aerodynamic stations. Inserting equation (B.2) into equation (B.1), and using equation (15), the final aerodynamic state equation as a function of the external input and structural deformations becomes:

$$\begin{bmatrix} \dot{\mathbf{\Gamma}}_{\mathbf{w}} \\ \dot{\boldsymbol{\alpha}}_{\mathbf{air}} \end{bmatrix} = \underbrace{\begin{bmatrix} \mathbf{K_1} & \mathbf{K_2} & \frac{\sin\alpha_0}{V_\infty}\mathbf{K_2B_\alpha T_{SA}} & -\frac{\cos\alpha_0}{V_\infty}\mathbf{K_2B_\alpha T_{SA}} & \mathbf{K_2B_\alpha T_{SA}} & \mathbf{K_2B_{pitch}T_{SA}} \\ \mathbf{0} & \mathbf{0} & \mathbf{0} & \mathbf{0} & \mathbf{0} & \end{bmatrix}}_{\mathbf{H_1}} \begin{bmatrix} \mathbf{\Gamma}_{\mathbf{w}} \\ \boldsymbol{\alpha}_{\mathbf{air}} \\ \dot{\boldsymbol{\delta}}_{\mathbf{x_s}} \\ \dot{\boldsymbol{\delta}}_{\mathbf{z_s}} \\ \boldsymbol{\theta}_{\mathbf{y_s}} \\ \dot{\boldsymbol{\theta}}_{\mathbf{y_s}} \end{bmatrix} + \underbrace{\begin{bmatrix} \mathbf{0} \\ \mathbf{I} \end{bmatrix}}_{\mathbf{H_2}} \dot{\boldsymbol{\alpha}}_{\mathbf{air}} \tag{B.3}$$

Similarly the aerodynamic output vector can be related to the free stream perturbation angle of attack and the structural degrees of freedom, resulting in:

$$\mathbf{F_a} = \underbrace{\begin{bmatrix} \mathbf{L_1} & \mathbf{L_2} & \frac{\sin\alpha_0}{V_\infty}\mathbf{L_2B_\alpha T_{SA}} & -\frac{\cos\alpha_0}{V_\infty}\mathbf{L_2B_\alpha T_{SA}} & \mathbf{L_2B_\alpha T_{SA}} & (\mathbf{L_2B_{pitch}} + \mathbf{L_3B_\alpha})\,\mathbf{T_{SA}} \end{bmatrix}}_{\mathbf{H_3}} \begin{bmatrix} \mathbf{\Gamma}_{\mathbf{w}} \\ \boldsymbol{\alpha}_{\mathbf{air}} \\ \dot{\boldsymbol{\delta}}_{\mathbf{x_s}} \\ \dot{\boldsymbol{\delta}}_{\mathbf{z_s}} \\ \boldsymbol{\theta}_{\mathbf{y_s}} \\ \dot{\boldsymbol{\theta}}_{\mathbf{y_s}} \end{bmatrix}$$

$$+ \underbrace{\begin{bmatrix} \frac{\sin\alpha_0}{V_\infty}\mathbf{L_3B_\alpha T_{SA}} & -\frac{\cos\alpha_0}{V_\infty}\mathbf{L_3B_\alpha T_{SA}} & \mathbf{L_3B_{pitch}T_{SA}} \end{bmatrix}}_{\mathbf{H_4}} \begin{bmatrix} \ddot{\boldsymbol{\delta}}_{\mathbf{z_s}} \\ \ddot{\boldsymbol{\delta}}_{\mathbf{x_s}} \\ \ddot{\boldsymbol{\theta}}_{\mathbf{y_s}} \end{bmatrix} + \mathbf{L_3B_\alpha}\dot{\boldsymbol{\alpha}}_{\mathbf{air}} \tag{B.4}$$

(B.5)

Introducing the aeroelastic state vector, defined by $\mathbf{x} = \begin{bmatrix} \mathbf{\Gamma}_{\mathbf{w}} & \boldsymbol{\alpha}_{\mathbf{air}} & \dot{\mathbf{p}} & \mathbf{p} \end{bmatrix}^T$, the aerodynamic part of the aeroelastic state-space system is given by:

$$\begin{bmatrix} \mathbf{\Gamma}_{\mathbf{w}} \\ \boldsymbol{\alpha}_{\mathbf{air}} \end{bmatrix} = \mathbf{H_1T_1x} + \mathbf{H_2}\dot{\boldsymbol{\alpha}}_{\mathbf{air}} \tag{B.6}$$

$$\mathbf{F_a} = \mathbf{H_3T_1x} + \mathbf{H_4T_2}\dot{\mathbf{x}}_{\mathbf{s}} + \mathbf{L_3B_\alpha}\dot{\boldsymbol{\alpha}}_{\mathbf{air}} \tag{B.7}$$

where $\mathbf{x_s}$ is the structural state vector, $\mathbf{T_1}$ selects $\begin{bmatrix} \mathbf{\Gamma}_{\mathbf{w}} & \boldsymbol{\alpha}_{\mathbf{air}} & \dot{\boldsymbol{\delta}}_{\mathbf{x_s}} & \dot{\boldsymbol{\delta}}_{\mathbf{z_s}} & \boldsymbol{\theta}_{\mathbf{y_s}} & \dot{\boldsymbol{\theta}}_{\mathbf{y_s}} \end{bmatrix}^T$ from the state vector, $\mathbf{x}$, and $\mathbf{T_2}$ selects $\begin{bmatrix} \ddot{\boldsymbol{\delta}}_{\mathbf{z_s}} & \ddot{\boldsymbol{\delta}}_{\mathbf{x_s}} & \ddot{\boldsymbol{\theta}}_{\mathbf{y_s}} \end{bmatrix}^T$ from the time derivative of structural state vector, $\dot{\mathbf{x}}_{\mathbf{s}}$.

Next, considering the structural system of equations given by equation (7), using equation (13), the structural state-space system becomes:

$$\begin{bmatrix} \ddot{\mathbf{p}} \\ \dot{\mathbf{p}} \end{bmatrix} = \underbrace{\begin{bmatrix} \mathbf{0} & -\mathbf{M}^{-1}\mathbf{K} \\ \mathbf{I} & \mathbf{0} \end{bmatrix}}_{\mathbf{A_s}} \underbrace{\begin{bmatrix} \dot{\mathbf{p}} \\ \mathbf{p} \end{bmatrix}}_{\mathbf{x_s}} + \underbrace{\begin{bmatrix} -\mathbf{M}^{-1} \\ \mathbf{0} \end{bmatrix}}_{\mathbf{B_s}} \mathbf{T_{AS}}\mathbf{R_{AS}}\mathbf{F_a} \tag{B.8}$$

where $\mathbf{R_{AS}}$ rotates the aerodynamic forces to the structural coordinate system. Introducing the aerodynamic output equation, given by equation (B.7), the structural state-space system can be rewritten as:

$$\underbrace{\left(\mathbf{I} - \mathbf{B_s}\mathbf{T_{AS}}\mathbf{R_{AS}}\mathbf{H_4}\mathbf{T_2}\right)}_{\mathbf{H_5}} \dot{\mathbf{x}}_\mathbf{s} = \underbrace{\left(\mathbf{A_s}\mathbf{T_3} + \mathbf{B_s}\mathbf{T_{AS}}\mathbf{R_{AS}}\mathbf{H_3}\mathbf{T_1}\right)}_{\mathbf{H_6}} \mathbf{x} + \underbrace{\mathbf{B_s}\mathbf{T_{AS}}\mathbf{R_{AS}}\mathbf{L_3}\mathbf{B_\alpha}}_{\mathbf{H_7}} \dot{\boldsymbol{\alpha}}_\mathbf{air} \tag{B.9}$$

$$\dot{\mathbf{x}}_\mathbf{s} = \mathbf{H_5}^{-1}\mathbf{H_6}\mathbf{x} + \mathbf{H_5}^{-1}\mathbf{H_7}\dot{\boldsymbol{\alpha}}_\mathbf{air} \tag{B.10}$$

Finally, combining equation (B.6) and equation (B.10), the aeroelastic state equation is obtained as:

$$\dot{\mathbf{x}} = \underbrace{\begin{bmatrix} \mathbf{H_1}\mathbf{T_1} \\ \mathbf{H_5}^{-1}\mathbf{H_6} \end{bmatrix}}_{\mathbf{A_{ss}}} \mathbf{x} + \underbrace{\begin{bmatrix} \mathbf{H_4} \\ \mathbf{H_5}^{-1}\mathbf{H_7} \end{bmatrix}}_{\mathbf{B_{ss}}} \dot{\boldsymbol{\alpha}}_\mathbf{air} \tag{B.11}$$

In order to complete the dynamic aeroelastic state-space system, equation (B.10) is introduced in equation (B.7), to obtain the aerodynamic forces as a function of the aeroelastic states, resulting in:

$$\mathbf{F_a} = \underbrace{\left(\mathbf{H_3}\mathbf{T_1} + \mathbf{H_3}\mathbf{T_2}\mathbf{H_5}^{-1}\mathbf{H_6}\right)}_{\mathbf{H_8}} \mathbf{x} + \underbrace{\mathbf{H_4}\mathbf{T_2}\mathbf{H_5}^{-1}\mathbf{H_7} + \mathbf{L_3}\mathbf{B_\alpha}}_{\mathbf{H_9}} \dot{\boldsymbol{\alpha}}_\mathbf{air} \tag{B.12}$$

Including the structural degrees of freedoms as extra outputs, and rotating the aerodynamic forces to the structural coordinate system for consistency, the aeroelastic output equation becomes:

$$\begin{bmatrix} \mathbf{F} \\ \mathbf{p} \end{bmatrix} = \underbrace{\begin{bmatrix} \mathbf{R_{AS}}\mathbf{H_8} \\ \mathbf{T_4} \end{bmatrix}}_{\mathbf{C_{ss}}} \mathbf{x} + \underbrace{\begin{bmatrix} \mathbf{R_{AS}}\mathbf{H_9} \\ \mathbf{0} \end{bmatrix}}_{\mathbf{D_{ss}}} \dot{\boldsymbol{\alpha}}_\mathbf{air} \tag{B.13}$$

where $\mathbf{T_4}$ selects the structural degrees of freedom from the state vector.

References

[1] M. H. Shirk, T. J. Hertz, T. A. Weisshaar, Aeroelastic Tailoring Theory, Practice, and Promise, Journal of Aircraft 23 (1) (1986) 6–18. doi:10.2514/3.45260.

[2] T. J. Hertz, M. H. Shirk, R. H. Ricketts, T. A. Weisshaar, Aeroelastic tailoring with composites applied to forward swept wings, Tech. Rep. AFWAL-TR-81-3043, DTIC Document (1981).

[3] F. E. Eastep, V. A. Tischler, V. B. Venkayya, N. S. Khot, Aeroelastic Tailoring of Composite Structures, Journal of Aircraft 36 (6) (1999) 1041–1047. doi:10.2514/2.2546.

[4] M. Kameyama, H. Fukunaga, Optimum design of composite plate wings for aeroelastic characteristics using lamination parameters, Computers & Structures 85 (3-4) (2007) 213–224. doi:10.1016/J.Compstruc.2006.08.051.

[5] S. Guo, Aeroelastic optimization of an aerobatic aircraft wing structure, Aerospace Science and Technology 11 (5) (2007) 396–404. doi:10.1016/J.Ast.2007.01.003.

[6] T. U. Kim, I. H. Hwang, Optimal design of composite wing subjected to gust loads, Computers & Structures 83 (19-20) (2005) 1546–1554. doi:10.1016/J.Compstruc.2005.02.002.

[7] G. A. Georghiades, S. J. Guo, J. R. Banerjee, Flutter characteristics of laminated composite wings, Journal of Aircraft 33 (6) (1996) 1204–1206. doi:10.2514/3.47078.

[8] S. J. Guo, J. R. Bannerjee, C. W. Cheung, The effect of laminate lay-up on the flutter speed of composite wings, Proceedings of the Institution of Mechanical Engineers Part G: Journal of Aerospace Engineering 217 (G3) (2003) 115–122. doi:10.1243/095441003322297225.

[9] T. A. Weisshaar, D. K. Duke, Induced drag reduction using aeroelastic tailoring with adaptive control surfaces, Journal of Aircraft 43 (1) (2006) 157–164. doi:10.2514/1.12040.

[10] Z. M. Qin, L. Librescu, P. Marzocca, Aeroelasticity of composite aerovehicle wings in supersonic flows, Journal of Spacecraft and Rockets 40 (2) (2003) 162–173. doi:10.2514/2.3950.

[11] F. H. Gern, L. Librescu, Aeroelastic tailoring of composite wings exhibiting nonclassical effects and carrying external stores, Journal of Aircraft 37 (6) (2000) 1097–1104. doi:10.2514/2.2718.

[12] G. A. A. Thuwis, R. Breuker, M. M. Abdalla, Z. Gürdal, Aeroelastic tailoring using lamination parameters, Structural and Multidisciplinary Optimization 41 (4) (2009) 637–646. doi:10.1007/s00158-009-0437-6.

[13] L. Librescu, A. Khdeir, Aeroelastic divergence of swept-forward composite wings including warping restraint effect, AIAA Journal 26 (11) (1988) 1373–1377.

[14] L. Librescu, J. Simovich, General formulation for the aeroelastic divergence of composite swept-forward wing structures, Journal of Aircraft 25 (4) (1988) 364–371.

[15] L. Librescu, O. Song, On the static aeroelastic tailoring of composite aircraft swept wings modelled as thin-walled beam structures, Composite Engineering 2 (5-7) (1992) 497–512.

[16] Z. Qin, P. Marzocca, L. Librescu, Aeroelastic instability and response of advanced aircraft wings at subsonic flight speeds, Aerospace Science and Technology 6 (2002) 195–208.

[17] J. K. S. Dillinger, T. Klimmek, M. M. Abdalla, Z. Gürdal, Stiffness Optimization of Composite Wings with Aeroelastic Constraints, Journal of Aircraft 50 (4) (2013) 1159–1168. doi:10.2514/1.C032084.

[18] O. Stodieck, J. E. Cooper, P. M. Weaver, P. Kealy, Improved aeroelastic tailoring using tow-steered composites, Composite Structures 106 (2013) 703–715. doi:10.1016/J.Compstruct.2013.07.023.

[19] B. K. Stanford, C. V. Jutte, K. Chauncey Wu, Aeroelastic benefits of tow steering for composite plates, Composite Structures 118 (2014) 416–422. doi:10.1016/j.compstruct.2014.08.007.

[20] B. K. Stanford, C. V. Jutte, C. D. Wieseman, Trim and Structural Optimization of Subsonic Transport Wings Using Nonconventional Aeroelastic Tailoring, AIAA Journal 54 (1) (2016) 293–309. doi:10.2514/1.J054244.

[21] T. R. Brooks, G. Kennedy, J. Martins, High-fidelity Aerostructural Optimization of a High Aspect Ratio Tow-steered Wing, in: 57th AIAA/ASCE/AHS/ASC Structures, Structural Dynamics, and Materials Conference, American Institute of Aeronautics and Astronautics, San Diego, CA, USA, 2016.

[22] H. Arizono, K. Isogai, Application of genetic algorithm for aeroelastic tailoring of a cranked-arrow wing, Journal of Aircraft 42 (2) (2005) 493–499. doi:10.2514/1.392.

[23] S. J. Guo, W. Y. Cheng, D. G. Cui, Aeroelastic tailoring of composite wing structures by laminate layup optimization,

Aiaa Journal 44 (12) (2006) 3146–3150. doi:10.2514/1.20166.

[24] A. Manan, G. A. Vio, M. Y. Harmin, J. E. Cooper, Optimization of aeroelastic composite structures using evolutionary algorithms, Engineering Optimization 42 (2) (2010) 171–184. doi:10.1080/03052150903104358.

[25] G. J. Kennedy, G. K. W. Kenway, J. R. R. Martins, A Comparison of Metallic, Composite and Nanocomposite Optimal Transonic Transport Wings, Tech. Rep. NASA CR-2014-0218185 (2014).

[26] N. Werter, R. De Breuker, M. M. Abdalla, Continuous-time state-space unsteady aerodynamic modelling for efficient aeroelastic load analysis, in: International Forum on Structural Dynamics and Aeroelasticity, St. Petersburg, Russia, 2015.

[27] E. Ferede, M. Abdalla, Cross-sectional modelling of thin-walled composite beams, in: Proceedings of 55th AIAA/ASME/ASCE/AHS/SC Structures, Structural Dynamics, and Materials Conference, American Institute of Aeronautics and Astronautics, 2014. doi:10.2514/6.2014-0163.

[28] R. De Breuker, M. M. Abdalla, Z. Gürdal, A Generic Morphing Wing Analysis and Design Framework, Journal of Intelligent Material Systems and Structures 22 (10) (2011) 1025–1039. doi:10.1177/1045389x11414958.

[29] J. Weissinger, The lift distribution of swept-back wings, Tech. Rep. NACA-TM-1120 (1947).

[30] R. Chandra, A. D. Stemple, I. Chopra, Thin-walled composite beams under bending, torsional, and extensional loads, Journal of Aircraft 27 (7) (1990) 619–626. doi:10.2514/3.25331.

[31] C. E. S. Cesnik, D. H. Hodges, VABS: A New Concept for Composite Rotor Blade CrossSectional Modeling, Journal of the American Helicopter Society 42 (1) (1997) 27–38. doi:10.4050/JAHS.42.27.

[32] V. V. Volovoi, D. H. Hodges, Theory of Anisotropic Thin-Walled Beams, Journal of Applied Mechanics 67 (3) (2000) 453–459. doi:10.1115/1.1312806.

[33] J.-M. Battini, C. Pacoste, Co-rotational beam elements with warping effects in instability problems, Computer Methods in Applied Mechanics and Engineering 191 (1718) (2002) 1755–1789. doi:10.1016/S0045-7825(01)00352-8.

[34] K.-J. Bathe, S. Bolourchi, Large displacement analysis of three-dimensional beam structures, International Journal for Numerical Methods in Engineering 14 (7) (1979) 961–986.

[35] M. A. Crisfield, A consistent co-rotational formulation for non-linear, three-dimensional, beam-elements, Computer methods in applied mechanics and engineering 81 (2) (1990) 131–150.

[36] J. Katz, A. Plotkin, Low-Speed Aerodynamics, Cambridge University Press, Cambridge, 2001.

[37] J. Murua, R. Palacios, J. M. R. Graham, Assessment of Wake-Tail Interference Effects on the Dynamics of Flexible Aircraft, AIAA Journal 50 (7) (2012) 1575–1585. doi:10.2514/1.J051543.

[38] L. Chen, H. Chern, The Vibrations of Pre-Twisted Rotating Beams of General Orthotropy, Journal of Sound and Vibration 167 (3) (1993) 529–539.

[39] M. Sabuncu, K. Evran, Dynamic stability of a rotating pre-twisted asymmetric cross-section Timoshenko beam subjected to an axial periodic force, International Journal of Mechanical Sciences 48 (6) (2006) 579–590. doi:10.1016/j.ijmecsci.2006.01.010.

[40] T.-N. Le, J.-M. Battini, M. Hjiaj, A consistent 3d corotational beam element for nonlinear dynamic analysis of flexible structures, Computer Methods in Applied Mechanics and Engineering 269 (2014) 538–565. doi:10.1016/j.cma.2013.11.007.

[41] M. Goland, The Flutter of a Uniform Cantilever Wing, Journal of Applied Mechanics 12 (4) (1945) A197–A208.

[42] Z. Wang, P. C. Chen, D. D. Liu, D. T. Mook, M. J. Patil, Time Domain Nonlinear Aeroelastic Analysis for HALE Wings, in: 47th AIAA/ASME/ASCE/AHS/ASC Structures, Structural Dynamics, and Materials Conference, American Institute of Aeronautics and Astronautics, Newport, 2006.

[43] M. J. Patil, D. H. Hodges, On the importance of aerodynamic and structural geometrical nonlinearities in aeroelastic behavior of high-aspect-ratio wings, Journal of Fluids and Structures 19 (7) (2004) 905–915.

doi:10.1016/j.jfluidstructs.2004.04.012.

[44] H. L. Runyan, J. L. Sewall, Experimental Investigation of the Effects of Concentrated Weights on Flutter Characteristics of a Straight Cantilever Wing, Tech. Rep. NACA-TN-1594, NACA (1948).

[45] S. A. Fazelzadeh, A. Mazidi, H. Kalantari, Bending-torsional flutter of wings with an attached mass subjected to a follower force, Journal of Sound and Vibration 323 (12) (2009) 148–162. doi:10.1016/j.jsv.2009.01.002.

[46] Z. Wang, P. C. Chen, D. D. Liu, D. T. Mook, Nonlinear-Aerodynamics/Nonlinear-Structure Interaction Methodology for a High-Altitude Long-Endurance Wing, Journal of Aircraft 47 (2) (2010) 556–566. doi:10.2514/1.45694.

[47] V. Hammer, M. Bendse, R. Lipton, P. Pedersen, Parametrization in laminate design for optimal compliance, International Journal of Solids and Structures 34 (4) (1997) 415–434.

[48] M. W. Bloomfield, C. G. Diaconu, P. M. Weaver, On feasible regions of lamination parameters for lay-up optimization of laminated composites, Proceedings of the Royal Society of London A: Mathematical, Physical and Engineering Sciences 465 (2104) (2009) 1123–1143. doi:10.1098/rspa.2008.0380.

[49] S. Setoodeh, M. Abdalla, Z. Gürdal, Approximate Feasible Regions for Lamination Parameters, in: 11th AIAA/ISSMO Multidisciplinary Analysis and Optimization Conference, American Institute of Aeronautics and Astronautics, Portsmouth, VA, USA, 2006.

[50] Z. Wu, G. Raju, P. M. Weaver, Framework for the Buckling Optimization of Variable-Angle Tow Composite Plates, AIAA Journal 53 (12) (2015) 3788–3804. doi:10.2514/1.J054029.

[51] K. Svanberg, A class of globally convergent optimization methods based on conservative convex separable approximations, SIAM Journal on Optimization 12 (2) (2002) 555–573.

Table B.1: Composite beam properties used for validation

Dimensions		Layup*		Material properties		Loading	
Length	0.762 m	Upper wall	$[45]_6$	E_{11}	141.96 GPa	Tip load	4.45 N
Width	0.0242 m	Lower wall	$[-45]_6$	E_{22}	9.79 GPa		
Height	0.0136 m	Right wall	$[45/-45]_3$	G_{12}	6.00 GPa		
		Left wall	$[45/-45]_3$	ν_{12}	0.42		
				t_{ply}	0.127 mm		

*Layup is defined with respect to the beam axis and positive with respect to the outward normal

Table B.2: Beam properties

Cross-sectional properties		Material properties		Loading		
Width	1 m	E	10 MPa	Tip	$F_z = 600$ N	$M_x = 0$ Nm
Height	1 m	G	5 MPa	Constant eccentric	$F_z = 600$ N	$M_x = -4000$ Nm
		ρ	1000 kg/m^3	Follower eccentric	$F_z = 300$ N	$M_x = -2500$ Nm

Table B.3: Comparison of the tip location (x,y,z) under various load levels

Load level	300	450	600
Present	22.12, 58.54, 40.48	18.37, 51.97, 48.70	15.56, 46.90, 53.60
Bathe and Bolourchi[34]	22.5, 59.2, 39.5	–	15.9, 47.2, 53.4
Crisfield[35]	22.16, 58.53, 40.53	18.43, 51.93, 48.79	15.61, 46.84, 53.71

Table B.4: HALE wing properties

Semispan	16 m
Chord	1 m
Elastic axis	50% chord
Center of gravity	50% chord
Mass per unit length	0.75 kg/m
Moment of inertia (around e.a.)	0.1 kgm
Torsional stiffness	$1 \cdot 10^4$ Nm^2
Bending stiffness	$2 \cdot 10^4$ Nm^2
Chordwise bending stiffness	$5 \cdot 10^6$ Nm^2

Table B.5: Eccentric mass properties

Mass	10 000 kg
I_{xx}	30 000 kgm^2
I_{yy}	50 000 kgm^2
I_{zz}	100 000 kgm^2

Table B.6: Goland wing properties

Semispan	6.096 m
Chord	1.8288 m
Elastic axis	33% chord
Center of gravity	43% chord
Mass per unit length	35.72 kg/m
Moment of inertia (around e.a.)	8.64 kgm
Torsional stiffness	$9.88 \cdot 10^5$ Nm^2
Bending stiffness	$9.77 \cdot 10^6$ Nm^2

Table B.7: Flutter speed of the Goland wing and a HALE aircraft wing

Goland			HALE		
	V_f	ω_f		V_f	ω_f
Wang et al.[42]	163.8 m/s	-	Patil et al.[43]	31.75 m/s	23.60 rad/s
ZAERO[42]	174.3 m/s	-	Murua et al.[37]	33 m/s	22 rad/s
Murua et al.[37]	165 m/s	69 rad/s	Present	32.12 m/s	23.21 rad/s
Present	168.4 m/s	69.4 rad/s			

Table B.8: Experimental wing properties[44]

Semispan	12.192 m
Chord	0.2032 m
Elastic axis	43.7% chord
Center of gravity	45.4% chord
Mass per unit length	1.2943 kg/m
Moment of inertia (around e.a.)	$3.56 \cdot 10^{-3}$ kgm
Torsional stiffness	198.6 Nm^2
Bending stiffness	403.8 Nm^2
Eccentric mass	1.44 kg
Chordwise location of the mass w.r.t. e.a.	−0.083 m
Moment of inertia (around mass c.g.)	$8.50 \cdot 10^{-3}$ kgm^2

Table B.9: Wing box properties

Spar locations			
Spanwise location	LE	Mid	TE
0 m	16.5 %chord	40.0 %chord	63.4 %chord
2.79 m	16.5 %chord	40.0 %chord	63.4 %chord
9.37 m	14.4 %chord	40.9 %chord	67.5 %chord
20.06 m	18.5 %chord	-	55.1 %chord
29.00 m	28.6 %chord	-	68.8 %chord

Table B.10: Non-structural mass

	Mass	x-location	y-location	z-location
Engine	8694.9 kg	−0.57 m	9.29 m	−1.50 m
Pylon	1688.5 kg	0.35 m	9.31 m	−0.44 m
Main landing gear	4463 kg	6.36 m	2.86 m	0.76 m

Table B.11: Fuel mass distribution

Fuel tanks		
Tank ID	Max. fuel mass	Spanwise location
1	17 000 kg	2.79 - 9.37 m
2	7500 kg	9.37 - 15.46 m
3	3000 kg	15.46 - 20.69 m
4	1500 kg	20.69 - 25.87 m
5	500 kg	25.87 - 29.00 m

Table B.12: Material properties

UD Carbon fibre	
E_{11}	83.0 GPa
E_{22}	8.5 GPa
G_{12}	4.2 GPa
ν_{12}	0.35
ρ	1452 kg/m^3
ϵ_{max}	4500 μstrain
γ_{max}	7000 μstrain

Table B.13: Optimisation setup

Objective	Minimum weight
Design variables	Lamination parameters
	Laminate thickness
Constraints	Laminate feasibility
	Aeroelastic stability
	Maximum local angle of attack
	Maximum principal strains
Optimiser	GCMMA

Table B.14: Load cases

ID	Description	EAS (m/s)	Altitude (m)	Mach	n_z	Fuel level (Tank 1-5)				
1	Begin Cruise	117.5	11900	0.78	1.0	0.5	1	1	1	0
2	End Cruise	117.5	11900	0.78	1.0	0	0	0.5	1	0
3	Symm. push down	162.4	7620	0.78	−1.0	0	0	0	0	0
4	Symm. pull up	178.1	7620	0.80	2.5	0	0	0	0	0
5	Symm. pull up	180.8	6096	0.69	2.5	0	0	0	0	0
6	Stability	222.0	−2300	0.57	1.0	0	0	0	0	0

Table B.15: Optimisation wing structural weight and corresponding cruise trim angle of attack

Case	Weight	Trim angle	
		Loadcase 1a	Loadcase 1b
Quasi-isotropic	2440 kg	4.42 deg	3.13 deg
Tailored	1164 kg	4.81 deg	3.50 deg

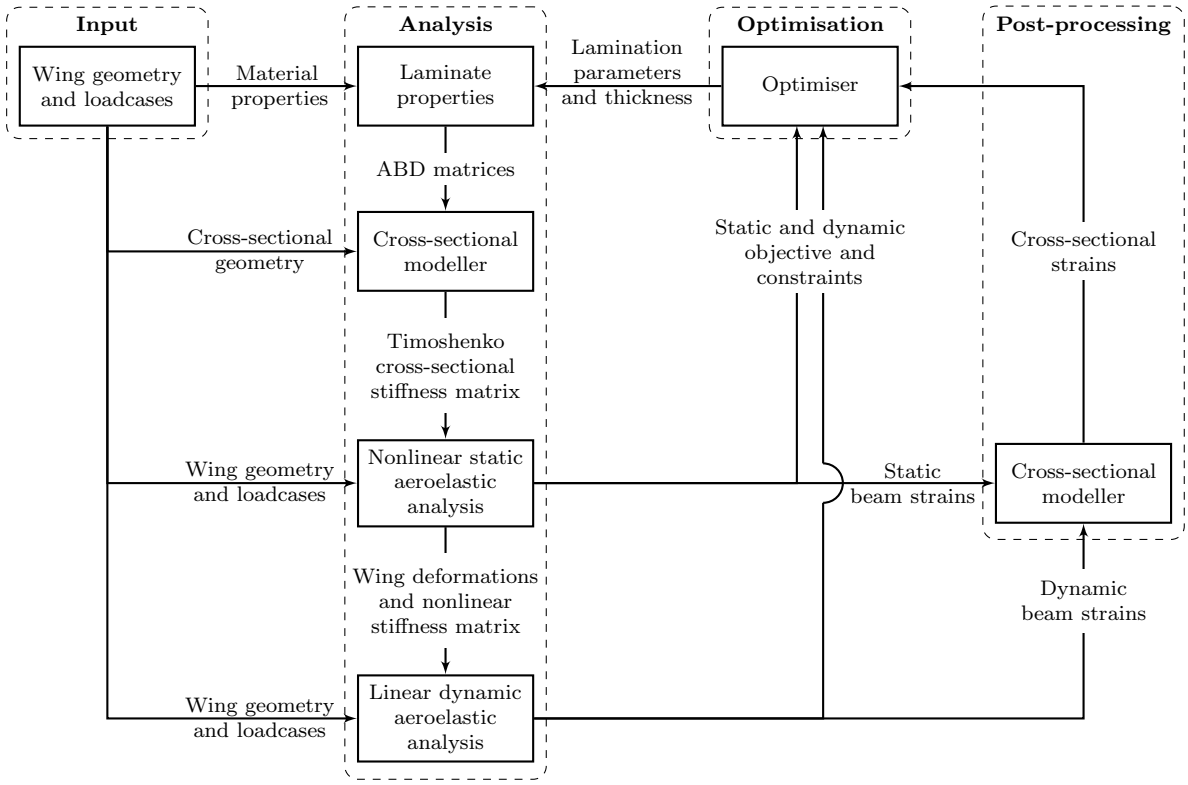

Figure B.1: Schematic representation of the aeroelastic analysis and optimisation loop.

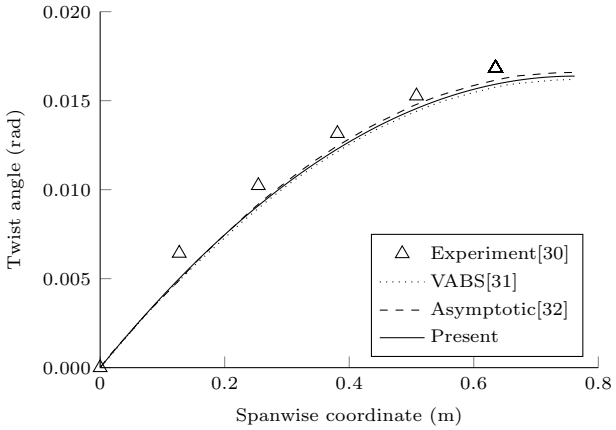

Figure B.2: Validation of the composite beam model with experiments and other numerical solutions.

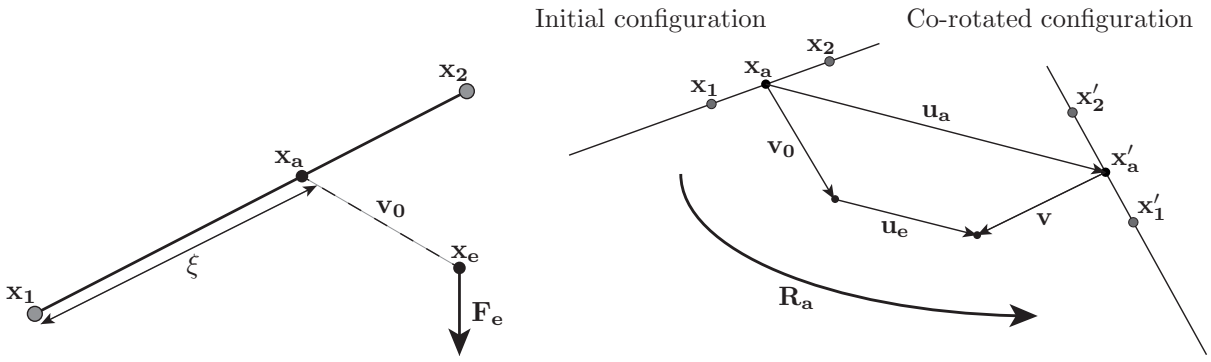

(a) Schematic illustration of an eccentric force or moment, $\mathbf{F_e}$, acting at location $\mathbf{x_e}$.

(b) Schematic illustration of the displacement of eccentric node, $\mathbf{x_e}$.

Figure B.3: Schematic illustration of the implementation of eccentric forces and moments.

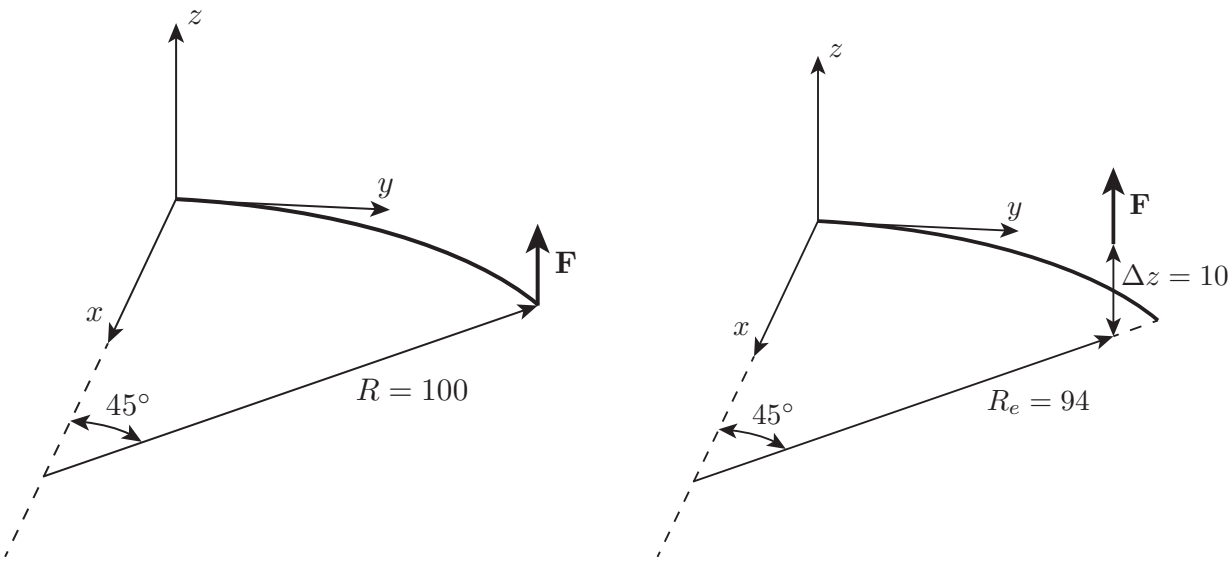

(a) Tip load **(b) Eccentric load**

Figure B.4: 45 deg circular bend under tip and eccentric load.

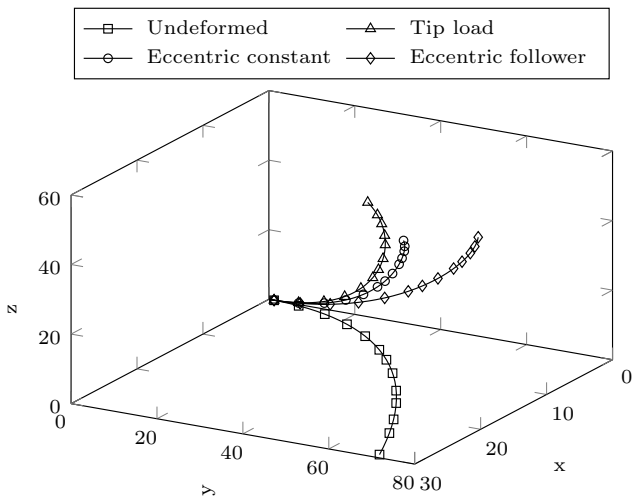

(a) Undeformed and deformed beam shape under different loads.

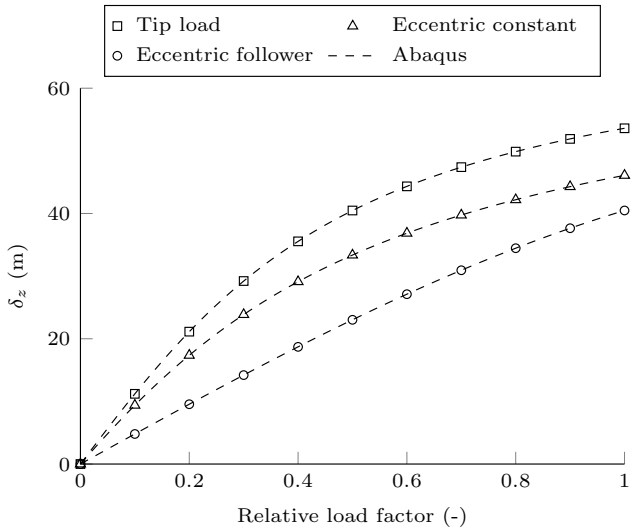

(b) Comparison of the out-of-plane tip displacement under different loads.

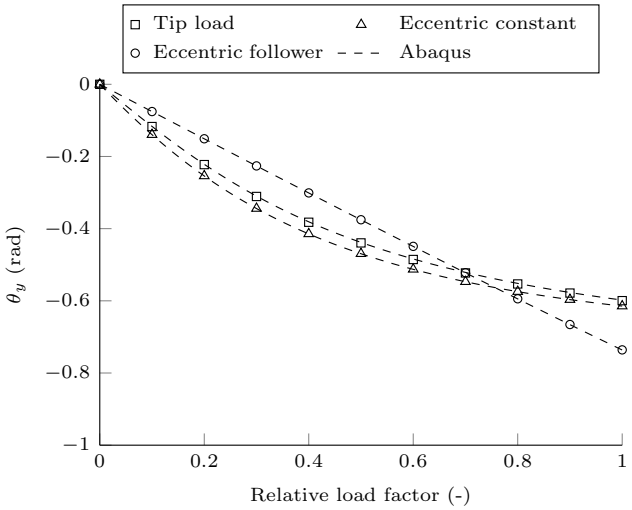

(c) Comparison of the rotation about the y-axis under different loads.

Figure B.5: Verification of the implementation of eccentric forces and moments

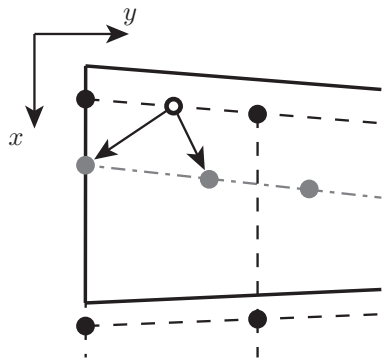

Figure B.6: Schematic illustration of the transfer of the aerodynamic forces, indicated with the open circles, to the structural nodes, indicated with the grey circles. The thick solid lines indicate the wing outline, the dashed lines indicate the vortex ring elements, the black circles indicate the vortex line vertices, and the thick gray line indicates the structural beam.

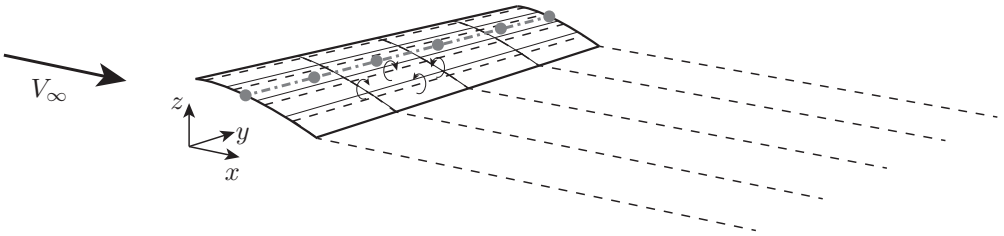

Figure B.7: Example wing discretization using vortex ring elements. The thick solid lines indicate the wing outline, the thin solid lines indicate the panel distribution, the dashed lines indicate the vortex ring elements, and the thick gray line indicates the structural beam.

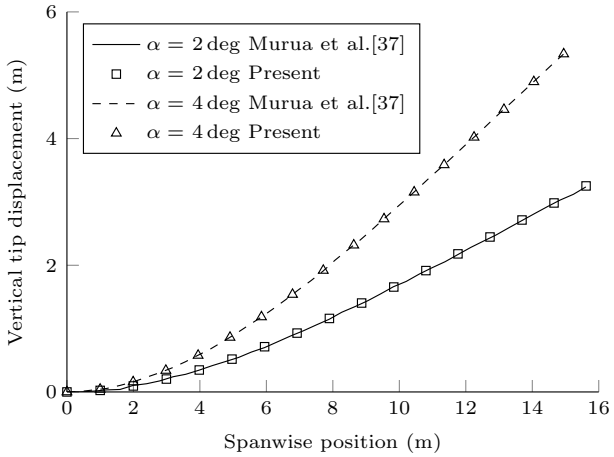

Figure B.8: Static aeroelastic deflection of a HALE aircraft wing under different angles of attack.

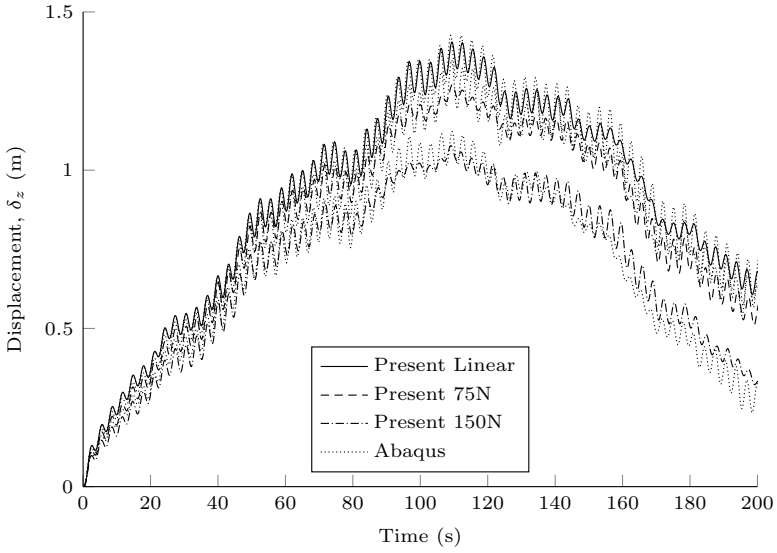

Figure B.9: Tip displacement around the nonlinear static equilibrium position under a time dependent tip load.

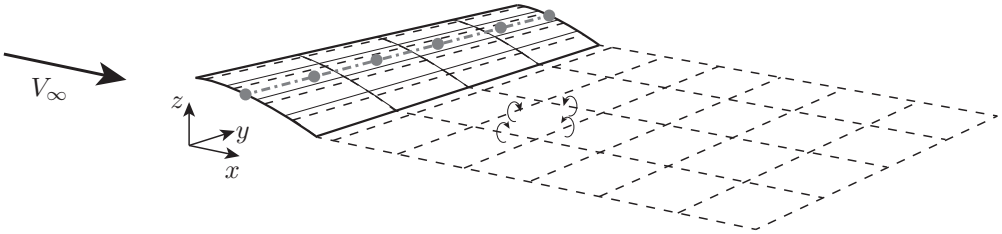

Figure B.10: Example wing and wake discretization using vortex ring elements. The thick solid lines indicate the wing outline, the thin solid lines indicate the panel distribution, the dashed lines indicate the vortex ring elements, and the thick gray line indicates the structural beam.

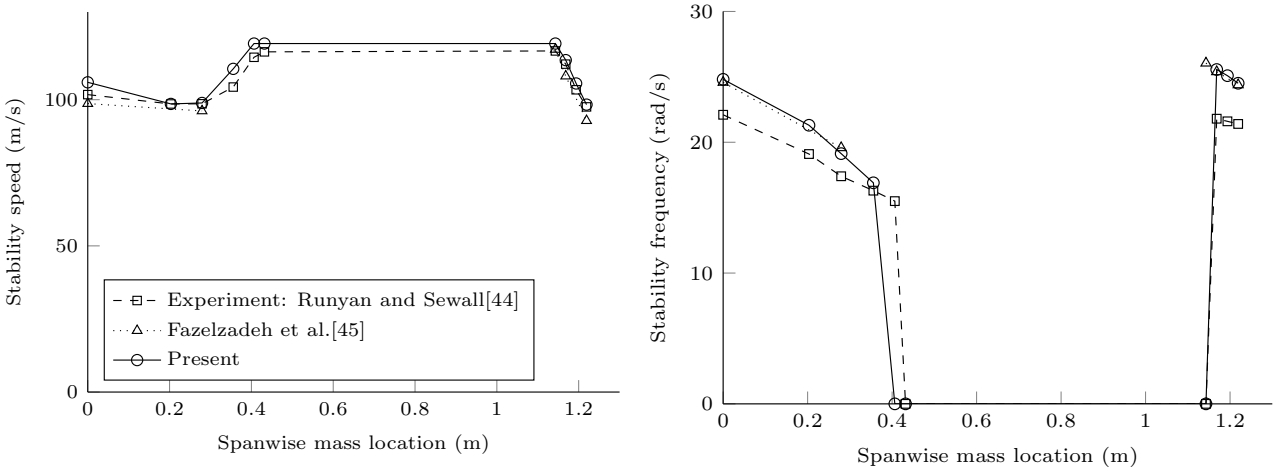

(a) Aeroelastic stability speed

(b) Aeroelastic stability frequency

Figure B.11: Aeroelastic stability speed and frequency of a wing with an eccentric mass at different spanwise locations.

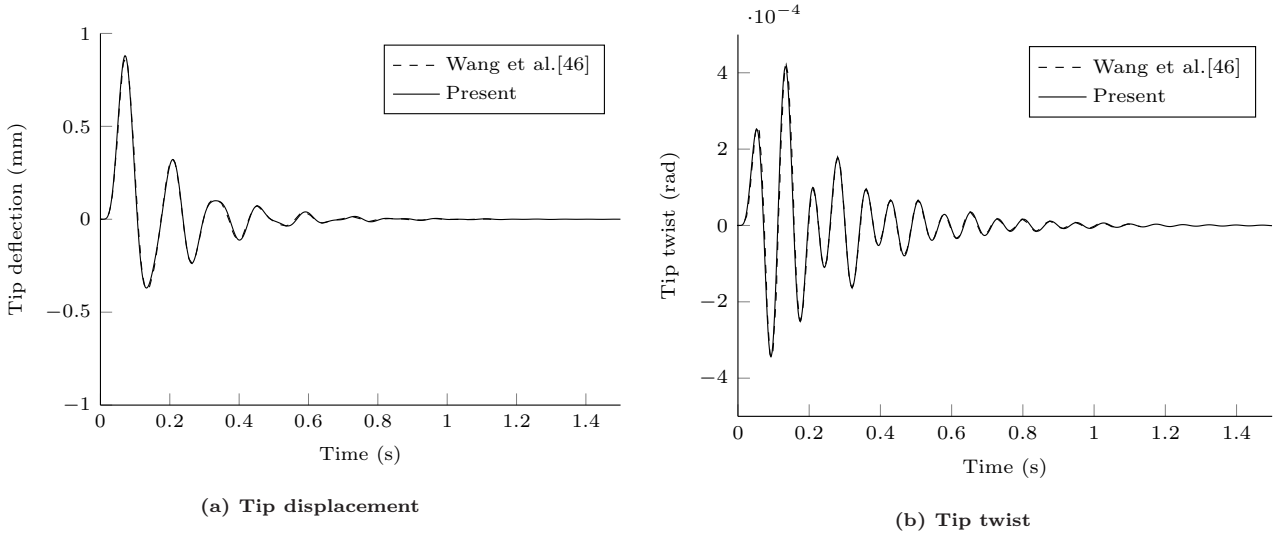

(a) Tip displacement

(b) Tip twist

Figure B.12: Gust response of the Goland wing under a 1-cosine gust.

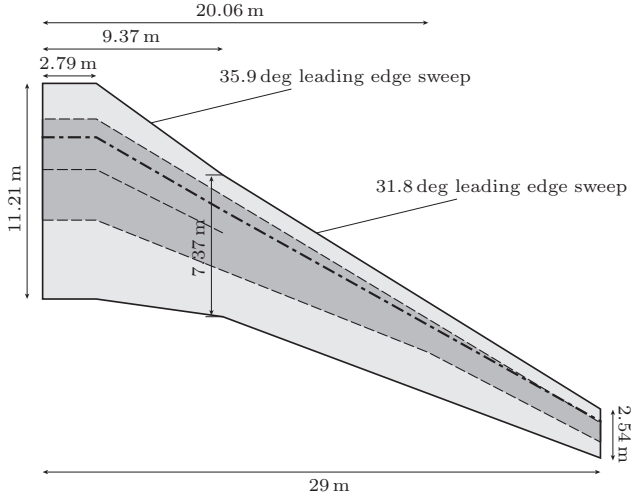

(a) Wing planform indicating the wingbox in dark grey, the spar locations by the dashed lines, and the beam reference axis by the dash-dotted line.

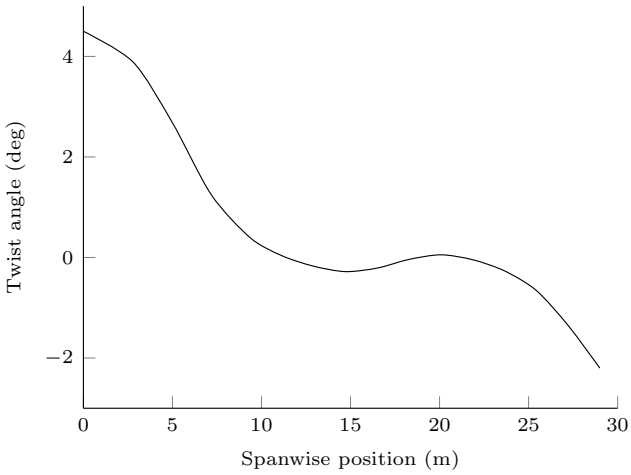

(b) Twist distribution

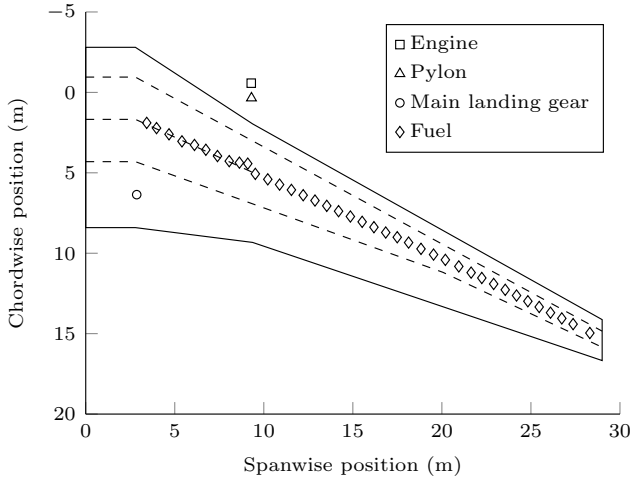

(c) Non-structural mass locations.

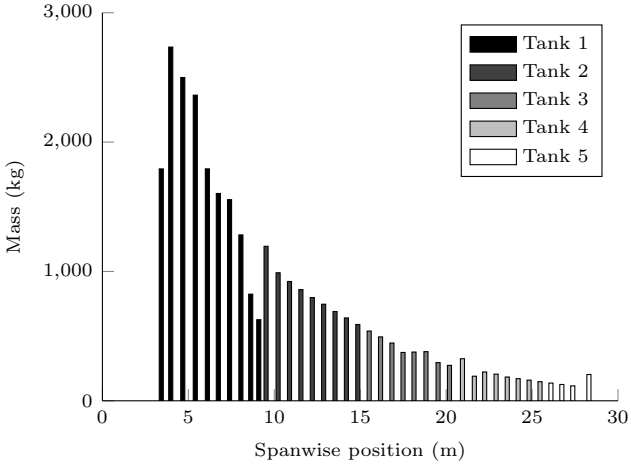

(d) Fuel mass distribution

Figure B.13: Wing properties

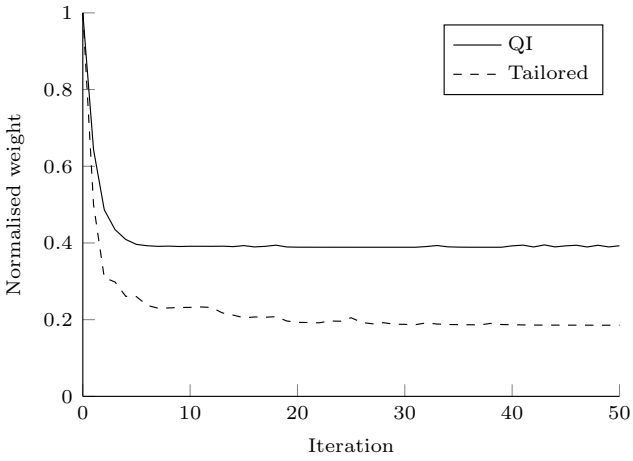

(a) Evolution of weight normalised with respect to the initial design

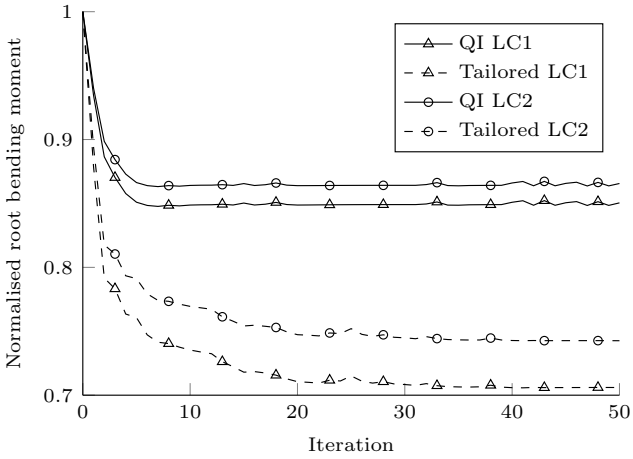

(b) Evolution of the root bending moment of load case 1 and load case 2 normalised with respect to the initial design

Figure B.14: Optimisation results

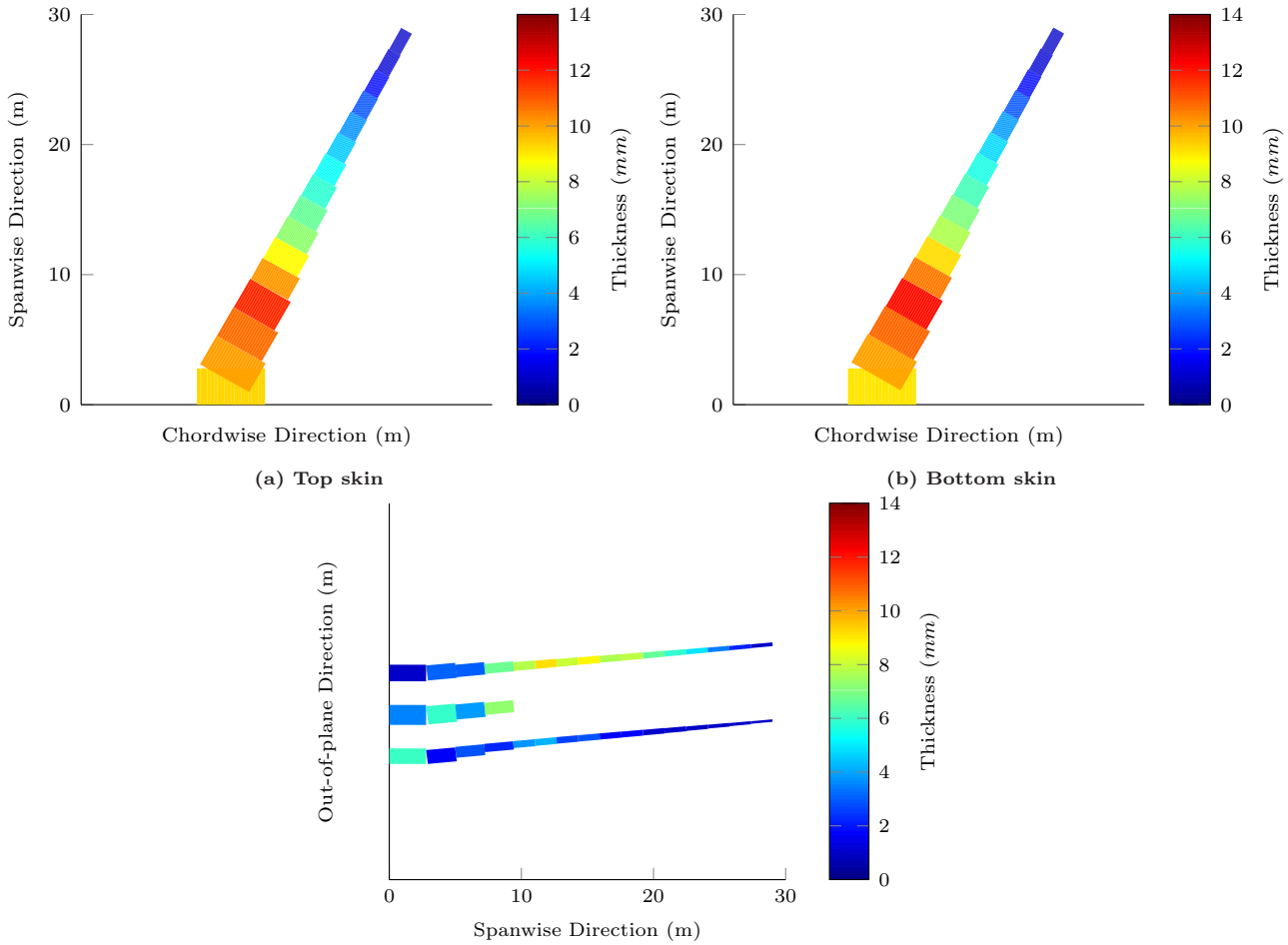

(a) Top skin

(b) Bottom skin

(c) Spars, LE to TE from top to bottom

Figure B.15: Quasi-isotropic wing thickness distribution.

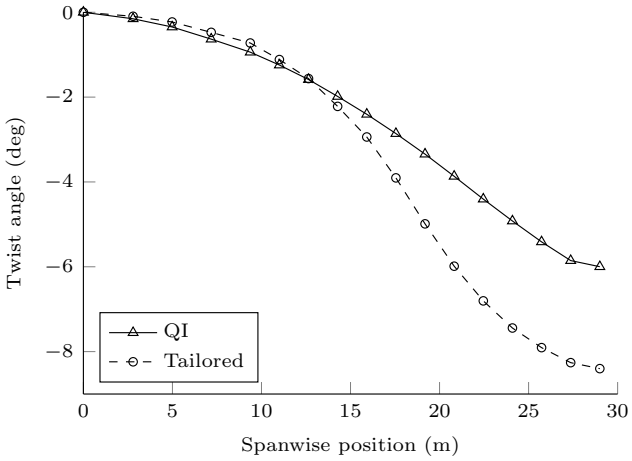

(a) Spanwise variation of the elastic twist for loadcase 1.

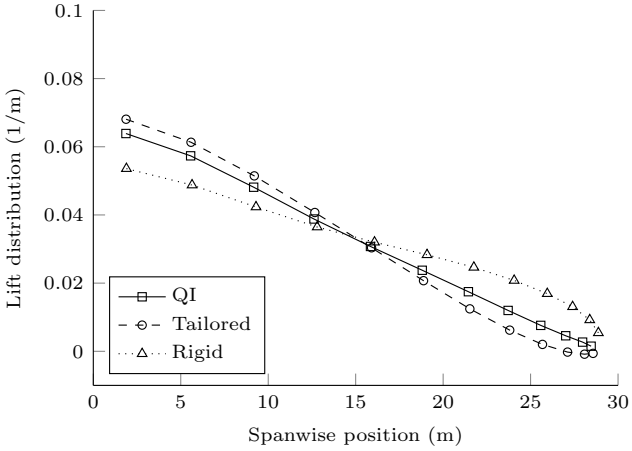

(b) Normalized lift distribution for loadcase 1.

Figure B.16: Optimised twist and lift distribution

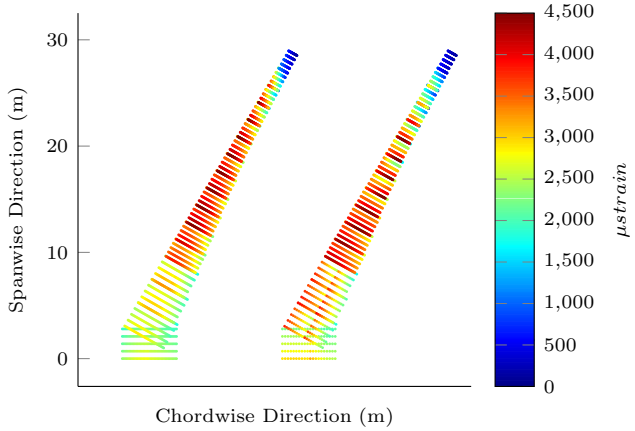

(a) ϵ_{max} of the quasi-isotropic wing (left) and the tailored wing (right) for load case 3.

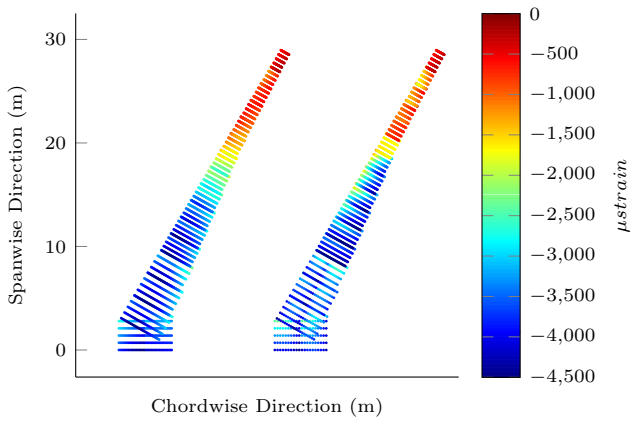

(b) ϵ_{min} of the quasi-isotropic wing (left) and the tailored wing (right) for load case 5.

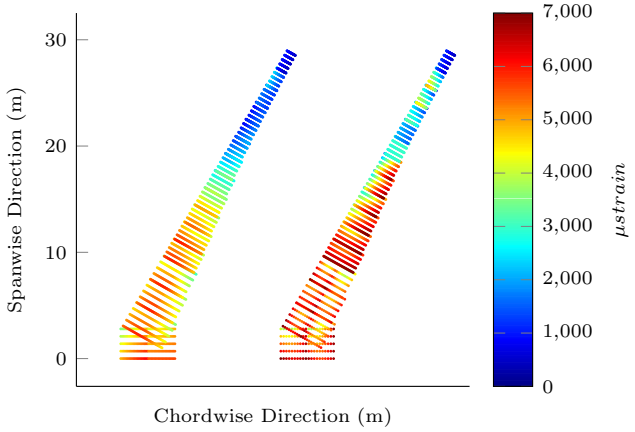

(c) γ of the quasi-isotropic wing (left) and the tailored wing (right) for load case 5.

Figure B.17: Strains on the top skin.

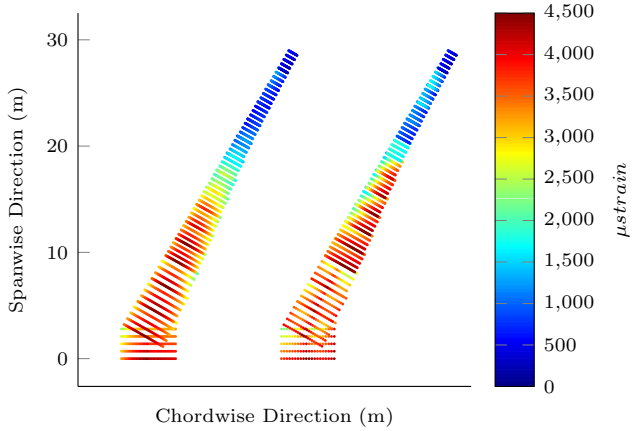

(a) ϵ_{max} of the quasi-isotropic wing (left) and the tailored wing (right) for load case 5.

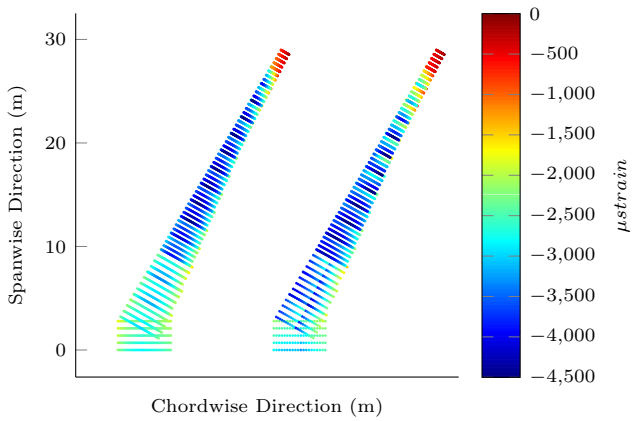

(b) ϵ_{min} of the quasi-isotropic wing (left) and the tailored wing (right) for load case 3.

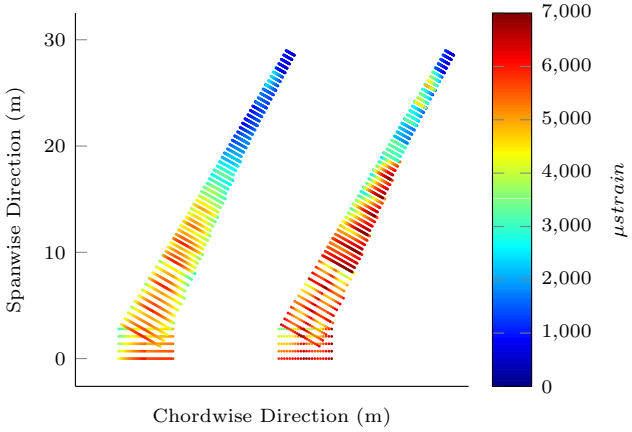

(c) γ of the quasi-isotropic wing (left) and the tailored wing (right) for load case 5.

Figure B.18: Strains on the bottom skin.

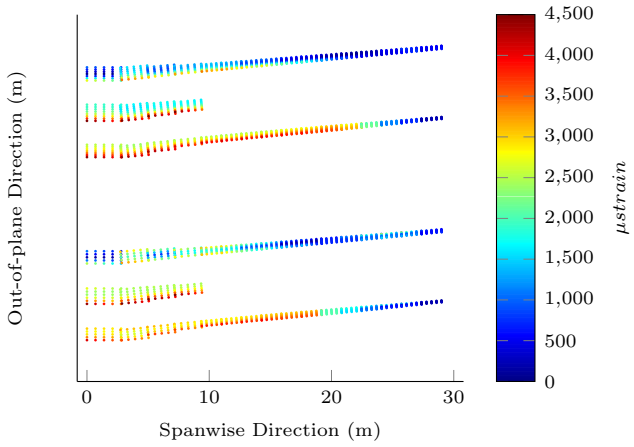

(a) ϵ_{max} of the spars of the quasi-isotropic wing (top three) and the tailored wing (bottom three) for load case 5, LE to TE from top to bottom.

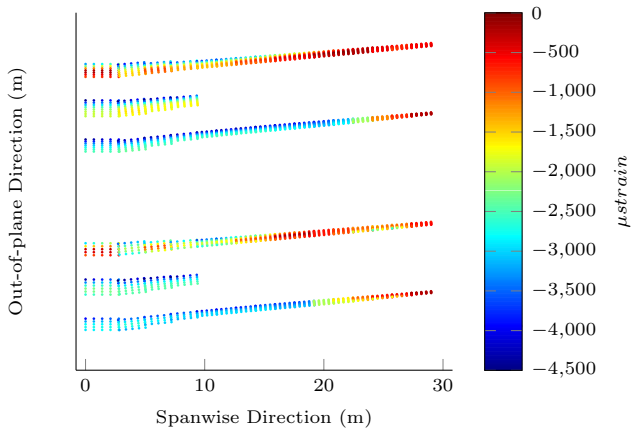

(b) ϵ_{min} of the spars of the quasi-isotropic wing (top three) and the tailored wing (bottom three) for load case 5, LE to TE from top to bottom.

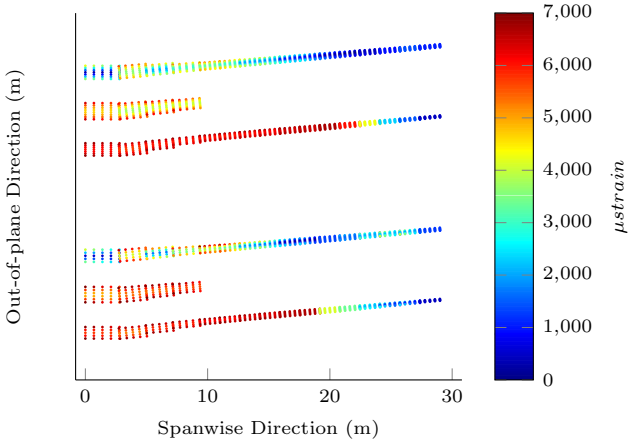

(c) γ of the quasi-isotropic wing (top three) and the tailored wing (bottom three) for load case 5, LE to TE from top to bottom

Figure B.19: Strains on the spars

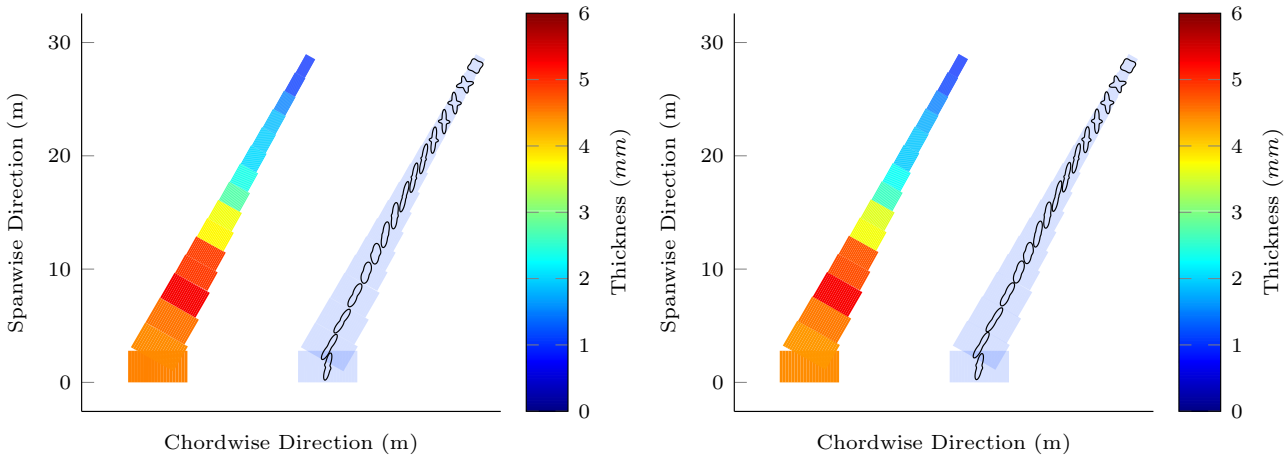

(a) Top skin (left: thickness, right: stiffness)

(b) Bottom skin (left: thickness, right: stiffness)

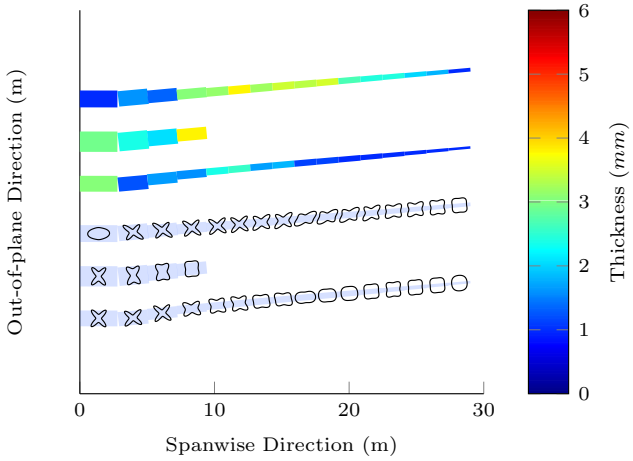

(c) Spars, LE to TE from top to bottom (top: thickness, bottom: stiffness)

Figure B.20: Tailored wing stiffness and thickness distribution.